

RESEARCH ARTICLE

10.1029/2018JE005563

Special Section:

Science and Exploration of the Moon, Near-Earth Asteroids, and the Moons of Mars

This article is a companion to Fiege et al. (2019) <https://doi.org/10.1029/2018JE005564>.

Key Points:

- This paper presents the modeling of micrometeoroid impacts on main belt and near-Earth asteroids
- The contribution of cometary, asteroidal, and interstellar dust as space weathering agents is evaluated

Correspondence to:

N. Altobelli,
nicolas.altobelli@sciops.esa.int

Citation:

Altobelli, N., Fiege, K., Carry, B., Soja, R., Guglielmino, M., Trieloff, M., et al. (2019). Space weathering induced via microparticle impacts: 1. Modeling of impact velocities and flux of micrometeoroids from cometary, asteroidal, and interstellar origin in the main asteroid belt and the near-Earth environment *Journal of Geophysical Research: Planets*, 124, 1044–1083. <https://doi.org/10.1029/2018JE005563>

Received 31 JAN 2018

Accepted 30 AUG 2018

Accepted article online 13 SEP 2018

Published online 29 APR 2019

Author Contributions

Writing - review & editing: B. Carry

Space Weathering Induced Via Microparticle Impacts: 1. Modeling of Impact Velocities and Flux of Micrometeoroids From Cometary, Asteroidal, and Interstellar Origin in the Main Asteroid Belt and the Near-Earth Environment

N. Altobelli¹, K. Fiege^{2,4}, B. Carry³, R. Soja⁴, M. Guglielmino², M. Trieloff², T. M. Orlando⁵, and R. Srama⁴

¹ESA, European Space Agency, Madrid, Spain, ²Klaus-Tschira-Labor für Kosmochemie, Institut für Geowissenschaften, Universität Heidelberg, Heidelberg, Germany, ³Université Côte d'Azur, Observatoire de la Côte d'Azur, CNRS, Laboratoire Lagrange, Nice, France, ⁴Institut für Raumfahrtssysteme, Universität Stuttgart, Stuttgart, Germany, ⁵School of Chemistry and Biochemistry, Georgia Institute of Technology, Atlanta, GA, USA

Abstract The processes of alteration of airless bodies exposed to the space environment are referred to be as “space weathering.” Multiple agents contribute generally to space weathering, to an extent that depends on the specific location of the surface within the solar system. Typical space weathering agents encountered in the solar system are solar radiation, solar wind and cosmic rays, magnetospheric plasma (e.g., at Jupiter or Saturn), and cosmic dust. The effect of space weathering is generally assessed by measuring the surfaces optical properties, for example, by near-infrared spectroscopy. The alteration of the surfaces is due to a cumulative effect over time of all agents. We investigate in this paper the contribution of micrometeoroid (dust) bombardment on different asteroids, by using the Interplanetary Micrometeoroid Environment Model for the interplanetary dust populations and a simplified model of interstellar dust dynamics. We quantify, for different representative asteroids (main belt and Near Earth Objects [NEOs]), the particle cumulative flux, mass flux, impact velocity, and the kinetic impact energy deposited. This work is primarily intended to support laboratory work investigating the effect of energy deposition onto sample surfaces, as well as astronomical observations of optical properties of asteroid surfaces.

Plain Language Summary This paper explores the impact speed, mass flux, and kinetic energy flux of interplanetary and interstellar micrometeoroids on near-earth and main belt asteroids from different dynamical families. This paper aims at providing constraints to current and future experimental work to understand the space weathering of asteroids surfaces induced by dust impacts. The simulations are performed using the latest version of the micrometeoroid environment model of the European Space Agency (Interplanetary Micrometeoroid Environment Model). We find that for all asteroids studied, the dust impactors deposit orders of magnitude less energy on the asteroid surfaces compared to the solar radiations but their contribution is comparable to that of heavy solar wind ions and electrons. We find that large cometary grains provide most of the mass flux delivered to asteroids surfaces, independently of the asteroids orbital elements, suggesting that dust bombardment is unlikely to play a significant role in driving the observed spectral trends among the different asteroids. While surface gardening by dust bombardment may, in turn, expose fresh material from the asteroid's surface, the required interplanetary dust population mass flux seems too low to efficiently counterbalance the surface weathering due to solar wind implantation.

1. Introduction

We investigate the characteristics of meteoroid impacts on the surface of asteroids with different orbital elements in order to support the experimental investigations of space weathering of asteroid surfaces (see Fiege et al., 2019). Space weathering is the process of alteration of exposed surfaces of objects throughout the solar system via the interaction with their environment (Bennett et al., 2013; Brunetto et al., 2015). Alteration is caused by weathering agents, such as energetic irradiation, stemming from a variety of sources (solar,

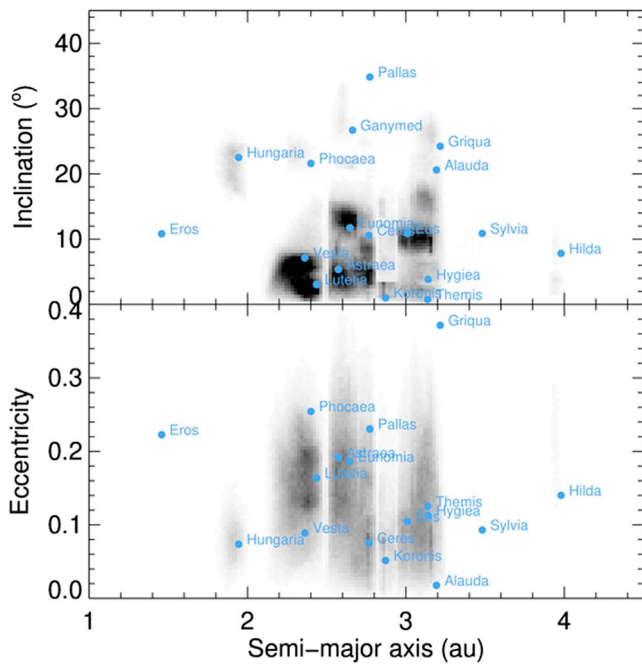


Figure 1. Main belt asteroids (black dots) plotted as function of their orbit's inclination (upper panel) and eccentricity (lower panel) versus the orbit's semimajor axis. The asteroids selected for this study are indicated by their name.

galactic, or magnetospheric), and meteoroid and micrometeoroid (hereafter referred to as “dust”) impacts. Understanding how energy is deposited by the different weathering agents on the surface of asteroids, and possibly changing their spectral type, is key to understand their origin and evolution. For example, alteration by the solar wind can process very rapidly to give its final “color” to an exposed surface, with the final reflectance properties being dependent on the original surface composition and on the surface-particle-size properties, such that color trends observed for different asteroids may not be directly linked to an exposition age (Vernazza et al., 2009). In parallel, rejuvenation processes, like gardening by micrometeorites impacts, can counteract the effect of solar wind irradiation by exposing fresh surface material.

Knowledge of the dust dynamics and size distribution at the location of the asteroids of interest is a prerequisite to quantify the exposition of their surface to micrometeoroid bombardment. Thanks to the investigations of various missions (e.g., Pioneer 10 and 11, Galileo, Helios, Ulysses, and Cassini; Grün et al., 1993), providing in situ data from onboard dust analyzers, dust fluxes have been assessed at various locations in the solar system. The dynamical evolution and the relative abundance of dust grains in the interplanetary space are determined by their interaction with solar gravity, radiation pressure, the coupling with the interplanetary magnetic field (IMF) through Lorentz forces, dynamical resonances with the giant planets, and mutual collisions.

Developing dust flux prediction models in the inner solar system has been an active field of research in the last decades (Dikarev et al., 2005; Divine, 1993; Grün et al., 1985; Staubach et al., 1997), and model improvements are still being worked on. In particular, the importance of cometary contribution to the inner solar system dust populations was empathized by Nesvorný et al. (2010). Modeling of the outer solar system dust fluxes was made possible only recently thanks to the new in situ dust data gathered by the New Horizon mission (Poppe, 2016). For this work, focusing on the dust bombardment of asteroid surfaces, we use the Interplanetary Micrometeoroid Environment Model (IMEM) by Dikarev et al. (2005), developed for the European Space Agency (ESA) to assess hazards caused by micrometeoroids to space missions. This model includes asteroidal and cometary dust populations coupled to an evolutionary model of their orbital elements in the inner solar system (see section 3).

2. Selection of Representative Asteroids

We selected a set of asteroids for our simulations, whose orbits cover a wide range of semimajor axis a , eccentricity e , and inclination i , such as to reflect the diversity of the different dynamical families within the main belt (Figure 1). We also selected three NEOs, including an example of very rare asteroids having retrograde orbit (2009 HC82). Note that we did not include Jupiter trojan asteroids in our selection, because the corresponding heliocentric distances correspond to the limit of applicability of the IMEM model (Dikarev et al., 2005). The ephemerides for each asteroid have been generated from the Jet Propulsion Laboratory (JPL) Small-Body Database Browser (<https://ssd.jpl.nasa.gov/x/spk.html>) and exported in Spice kernel format (spk) for our simulations. Table 1 provides a summary of the asteroids chosen to perform the dust impact computations, ordered by increasing semimajor axis. Figure 1 shows the distribution of the main belt asteroids selected in this work in the (a,e,i) space on top of the full content of the JPL small bodies database.

3. Modeling of the Interplanetary Dust Populations

The interplanetary dust complex, also called the “zodiacal cloud,” is made of dust grains of various origins. The main sources of dust in the interplanetary space are cometary activity (Nesvorný et al., 2010) and asteroid collisions. In addition, dust from the interstellar medium surrounding the solar system is known to penetrate the heliosphere and is also a population of the zodiacal cloud. We refer the reader to Grün et al. (1997)—for a review of the zodiacal dust complex.

Table 1

Names, Orbital Characteristics and Taxonomy of the Asteroids Chosen for the Simulations of Micrometeoroids Impacts

Asteroid name	Comment	Semimajor axis (AU)	Eccentricity	Inclination (deg)	Taxonomy
433 Eros	NEO (Amor group)	1.45	0.22	10.8	S
434 Hungaria	Inner Main Belt	1.94	0.07	22.5	Xe
4 Vesta	Inner Main Belt	2.36	0.08	7.1	V
21 Lutetia	Inner Main Belt	2.4	0.16	3.0	Xc
25 Phocaea	Inner Main Belt	2.4	0.25	21.6	S
343158-2009 HC82	NEO (Apollo group)	2.52	0.8	154.4	
5 Astraea	Middle Main Belt	2.57	0.19	5.3	S
1036 Ganymed	NEO (Amor group)	2.6	0.53	26.6	S
15 Eunomia	Middle Main Belt	2.64	0.18	11.7	K
2 Pallas	Middle Main Belt	2.7	0.23	34.1	B
1 Ceres	Middle Main Belt	2.76	0.07	10	C
158 Koronis	Outer Main Belt	2.86	0.05	1.0	S
221 Eos	Outer Main Belt	3.01	0.1	10.8	K
24 Themis	Outer Main Belt	3.12	0.13	0.75	C
10 Hygiea	Outer Main Belt	3.14	0.11	3.8	C
702 Alauda	Outer Main Belt	3.19	0.01	20.58	B
1362 Griqua	Outer Main Belt	3.21	0.37	24.2	B
87 Sylvia	Outer Main Belt	3.49	0.08	10.85	X
153 Hilda	Outer Main Belt	3.97	0.13	7.8	X

In order to estimate the abundances and dynamical properties of dust at the asteroids positions, we use the ESA meteoroid model (IMEM) as described in Dikarev et al. (2005). This model is a truly (dynamical) evolutionary model that considers the orbital elements of known interplanetary dust sources, in particular, comets and asteroids. The model computes the evolution of the orbital elements of the released particles, taking into account radiation pressure, Poynting-Robertson drag (the relativistic, tangential component of the radiation pressure), gravitation, and mutual collisions of particles. The simulated dust complex is assumed to have its properties (flux and orbital element distribution) to be axisymmetric with respect to the ecliptic axis. The mass of the simulated grains ranges from 10^{-18} g to 1 g, and the heliocentric distance up to which IMEM predictions can be made is 5 AU. Seventy-two different interplanetary dust populations originating from comets are included in the IMEM model, depending on their size range and source regions. Two main dynamical regimes are defined in the model (Dikarev et al., 2005)—“small” grains (those with a mass lower than 10^{-6} g) will evolve dynamically (in a mass-dependent way) under the influence of the Poynting-Robertson drag and will depart significantly from the orbit of their parent bodies, while “large” grains (those with a mass larger than 10^{-5} g) will tend to remain on orbits close to those of their parent bodies. Depending on the grain source and evolution process, four main extended sources of dust are referred to hereafter in this paper (following the IMEM nomenclature, as in Dikarev et al., 2005): “Asteroid collision [AC],” “Asteroid Poynting-Robertson [APR],” “Comet collisions [CC],” “Comet Poynting-Robertson [CPR].” Those two [AC] and [CC] collision categories correspond, roughly, to large asteroidal and cometary dust grains, while the two [APR] and [CPR] categories, whose dynamics is dominated by PR drag, correspond to the small asteroidal and cometary grains. The relative abundance of each population are weighted in the IMEM model using the infrared observations by COBE (Kelsall et al., 1998), in situ impact detections by Ulysses and Galileo (Grün et al., 1997), and the lunar crater size distribution (Grün et al., 1985). We note that the cometary dust populations implemented in this model are limited to the dust production by Jupiter family comets (JFCs). While those populations have been identified to be the most abundant cometary dust contribution in the inner solar system (Nesvorný et al., 2010; Pokorný et al., 2014), we discuss the consequences of this model limitation for our study in section 5.

3.1. Modeling of the Interstellar Dust Population

While the IMEM model also includes an interstellar dust (ISD) component, its modeling was deemed too simplistic for the purpose of this paper, and we developed a specific module. Detailed dynamical

considerations of ISD within the solar system can be found in Landgraf et al. (1999) and Sterken et al. (2013). We summarize here only the aspects relevant for our study.

The ISD grains are injected into the solar system as a collimated flux along the $79^\circ/-8^\circ$ downstream heliocentric direction (see Mann, 2010, for a review). Those particles are on hyperbolic orbits with respect to the Sun, and their dynamics in the interplanetary space is determined by the mass-dependent balance between radiation pressure, solar gravity, and Lorentz forces. The parameter β is defined as the ratio between radiation pressure and gravity and is independent of the grain distance to the Sun. If $\beta = 1$, particles keep the ecliptic direction of their injection into the solar system and behave as if there was no Sun. If $\beta < 1$, gravity dominates, resulting in an attractive radial force toward the Sun, and if $\beta > 1$, radiation pressure dominates, resulting in a repulsive radial force from the Sun. The ratio between the grain charge and its mass determines the strength of the coupling of the grain trajectory to the IMF, through the Lorentz forces. For grains in the micron size range and above, assuming silicate bulk material densities, radiation pressure and solar gravity dominate the grains dynamics. In the submicron size range, Lorentz forces induce a focusing/defocusing effect following the solar activity cycles (e.g., Landgraf et al., 1999; Sterken et al., 2013). An ISD stream was first detected by the Ulysses dust analyzer outside of the ecliptic plane (Grün et al., 1993), corresponding to a particle flux of $1.5 \times 10^{-4} \text{ m}^{-2}/\text{s}$. The stream fluctuations were monitored by the dust detectors onboard Galileo, Helios, and Cassini from 0.3 to 5 AU (Altobelli et al., 2005, 2006), and their theoretical modeling was confirmed. Note that in this work, while our ISD simulations take radiation pressure into account, we did not simulate the IMF coupling, which dominates the grains dynamics only for the smallest ISD grains owing to their large charge-to-mass ratio. Such grains are typically smaller than 0.2 microns, and, because the dynamic coupling with the IMF will alter their impact direction but will not change their impact speed significantly, those grains will not contribute significantly to the kinetic energy flux responsible of space weathering.

4. Interplanetary Dust Impactors: Methods and Simulation Results

This section provides the simulation results (impact speed range, particle number flux, mass, and kinetic energy flux) for the asteroidal and JFCs dust populations impacting the surface of the asteroids along their orbit. The radiant directions (apparent downstream directions of the impactors, as seen from the impacted body) that yield the highest flux and impact speeds vary with the asteroids orbital elements, and, for asteroids with high eccentricities, those directions will depend on the asteroid's true anomaly. For the practical purpose of this study, which aims at providing ranges of impact speeds and flux values to be used in experimental studies, we take into account the anisotropy of the impacting dust flux as follows:

1. For each asteroid, a coordinate frame is defined such as to have the X -axis pointed to the Sun, and the Y -axis is defined as the orthogonal projection of the asteroid's heliocentric velocity vector on the X -axis. The Z -axis completes the right-handed frame. Hence, in this frame, the longitude values represent the local time on the asteroid surface, and the latitude values are defined with respect to the orbital plane of the asteroid. This reference frame has the advantage to depend only on the asteroid orbital elements and can be applied to all asteroids selected in this work to derive the value ranges of dust impact speed and flux in the surface. In turn, body fixed reference frames, while allowing to study the anisotropy of the distribution of the impactors flux on an asteroid surface (a task beyond the scope of this work), have the drawback of depending on the proper definition of a rotation axis for each asteroid.
2. The asteroid's surface is divided in surface elements of size $10^\circ \times 10^\circ$ longitude-latitude and defined by their normal vector expressed in the coordinate frame defined above. Each surface element is "flown" through the IMEM dust populations for a full orbit. The extremum values of the impact speed and flux for all surface elements are retrieved over the full trajectory such that the values reported for each asteroid are independent of the impact direction.

We note that for all asteroids considered in this work, the relative velocities of the dust grains with the asteroids is so high and the asteroid mass so weak, which the effect of gravitation focusing on the impact flux can be neglected (Colombo et al., 1966).

4.1. Impact Speed and Particle Cumulative Fluxes

Each simulation performed covers a full orbit of the asteroid, the position of the asteroid on its orbits being parameterized by the true anomaly (the closest point to the Sun is reached at 0° and the farthest point at 180°). An example of the simulation results for the impact speed of the different IDP populations (section

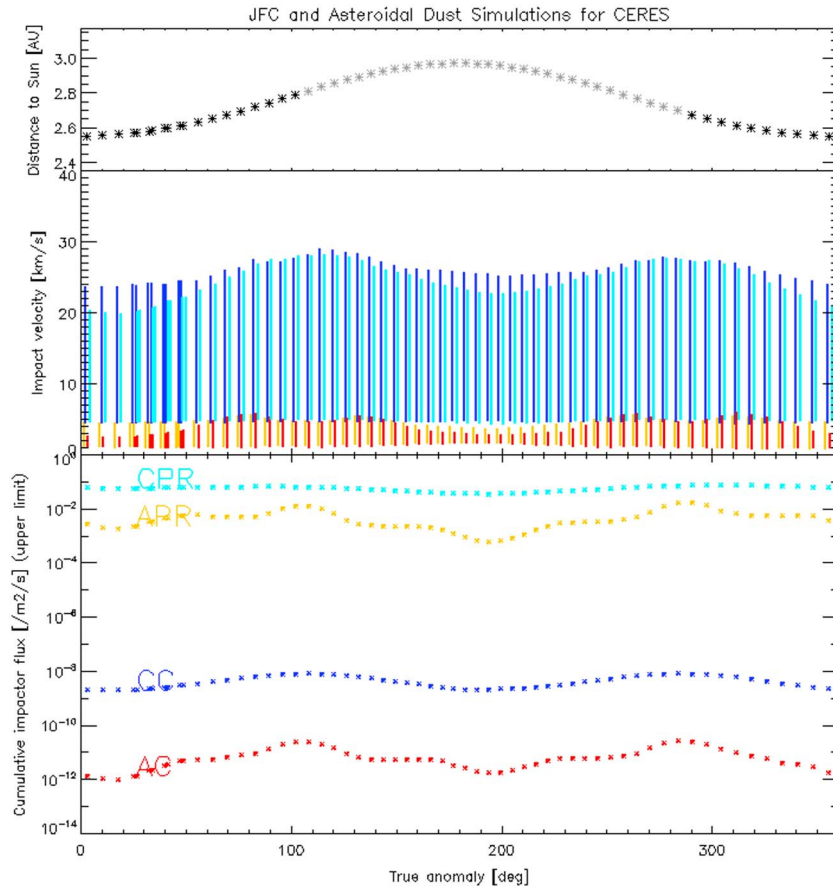


Figure 2. Flux and velocity of dust impactors on Ceres along its orbit. Top: distance of Ceres to the Sun in astronomical units as function of its true anomaly. The gray (black) symbols indicate when Ceres is located at southern (northern) ecliptic latitude. Middle: impact speed range. Bottom: maximum cumulative particle flux. The red and yellow colors in the middle and lower panels stand for the asteroidal asteroid collision (AC) and asteroid Poynting-Robertson (APR) dust populations, and the dark and light blue curves for the cometary comet collision (CC) and comet Poynting-Robertson (CPR) dust populations.

3), and their flux is shown for Ceres on Figure 2. The figures for each individual asteroid can be found in Appendix A. The flux values correspond to the cumulative flux in particle number belonging to each population. The differences between the impactors of cometary or asteroidal origin appear clearly in those plots, with a fast-speed impactor regime for cometary grains and a relatively low-speed impactor regime for asteroidal dust. Those differences in impact speed and the relative flux of the particles are discussed in section 5. In order to make the comparison of the dust impact speeds between different asteroids easier, we indicate the minimum and maximum values along the body's orbit in Table 2.

4.2. Kinetic Energy and Mass Flux

Of particular relevance for experimental studies of asteroid surface alteration by micrometeoroids impacts are the total mass flux and kinetic energy flux. Because both the particles dynamics, (and hence their impact speed on the asteroid surface), as well as the particles abundance (in terms of volume number density), are mass dependent, the simulations must be run within mass bins narrow enough to be able to consider the average particles velocity and abundance nearly independent of the mass within the mass bin. Practically, we have run for each asteroid 12 simulations covering logarithmically the mass range 10^{-12} to 1 g. The mass flux for each mass bin $Fm(M)$ is then derived by multiplying the middle mass value M of each interval with the corresponding particle flux, and the kinetic flux Ek is derived by evaluating $Ek(M) = \frac{1}{2} * M * v^2$, where v is the mean value of the impact speed of the particles within the mass bin. The total mass and kinetic energy fluxes are then obtained by summing up all contributions in all mass bins. Note that in order to facilitate the comparison of the kinetic energy deposited by micrometeoroids on asteroid surfaces with the value of other agents (solar wind particles and cosmic rays, e.g., such as those reported in Bennett et al., 2013; see

Table 2
Overview of the Minimum and Maximum Impact Speeds From the Asteroid Apex Direction for CD or AD

Asteroid name	CD Vmin (km/s)	CD Vmax (km/s)	AD Vmin (km/s)	AD Vmax (km/s)
EROS	14.7	36.2	10.7	17.9
HUNGARIA	18.8	39.8	6.5	15.1
VESTA	20.4	29.5	3.8	5.3
LUTETIA	18.5	27.4	3.7	5.4
PHOCAEA	16.9	39.5	5.0	13.6
HC82	18.7	110.1	13.7	111.6
ASTRAEA	18.3	27.6	4.5	5.8
GANYMED	17.1	46.2	6.0	22.3
EUNOMIA	17.0	31.7	4.9	7.0
PALLAS	25.1	44.1	7.9	16.3
CERES	19.9	29.1	2.5	5.9
KORONIS	18.7	24.5	2.9	3.2
EOS	21.8	30.1	2.9	6.2
THEMIS	16.5	26.2	2.1	4.1
HYGIEA	17.2	26.4	2.8	4.2
ALAUDA	25.8	35.8	6.1	8.4
GRIQUA	19.1	39.7	4.7	12.6
SYLVIA	20.3	29.7	3.3	8.4
HILDA	20.8	28.0	7.0	9.8

Note. CD = cometary dust; AD = asteroidal dust.

Table 3
Summary of the Minimum and Maximum IDP Mass and Kinetic Energy Flux Along the Orbit of the Different Asteroids

Asteroid name	Fm min ($\text{g}\cdot\text{cm}^{-2}\cdot\text{s}^{-1}$)	Fm max ($\text{g}\cdot\text{cm}^{-2}\cdot\text{s}^{-1}$)	Ek min ($\text{ev}\cdot\text{cm}^{-2}\cdot\text{s}^{-1}$)	Ek max ($\text{ev}\cdot\text{cm}^{-2}\cdot\text{s}^{-1}$)
EROS	8.2E-17	1.7E-16	3.5E+07	6.4E+07
HUNGARIA	8.2E-18	2.3E-16	4.2E+06	9.4E+07
VESTA	6.0E-17	1.1E-16	1.2E+07	2.5E+07
LUTETIA	8.1E-17	1.4E-16	1.3E+07	3.4E+07
PHOCAEA	5.9E-18	2.5E-16	4.2E+06	1.1E+08
HC82	1.8E-17	1.8E-15	2.1E+07	3.0E+10
ASTRAEA	8.6E-17	1.1E-16	1.3E+07	2.7E+07
GANYMED	6.0E-18	3.3E-16	4.9E+06	3.2E+08
EUNOMIA	3.0E-17	1.6E-16	8.6E+06	4.3E+07
PALLAS	2.1E-18	3.0E-16	2.2E+06	1.6E+08
CERES	3.4E-17	1.2E-16	7.1E+06	2.4E+07
KORONIS	7.7E-17	9.3E-17	1.3E+07	1.6E+07
EOS	4.0E-17	1.1E-16	7.2E+06	2.2E+07
THEMIS	7.2E-17	1.1E-16	1.6E+07	2.3E+07
HYGIEA	6.8E-17	1.1E-16	1.4E+07	2.4E+07
ALAUDA	7.7E-18	1.8E-16	5.7E+06	4.1E+07
GRIQUA	9.8E-18	2.7E-16	5.7E+06	1.2E+08
SYLVIA	3.1E-17	1.2E-16	8.3E+06	2.7E+07
HILDA	6.2E-17	1.2E-16	1.9E+07	4.7E+07

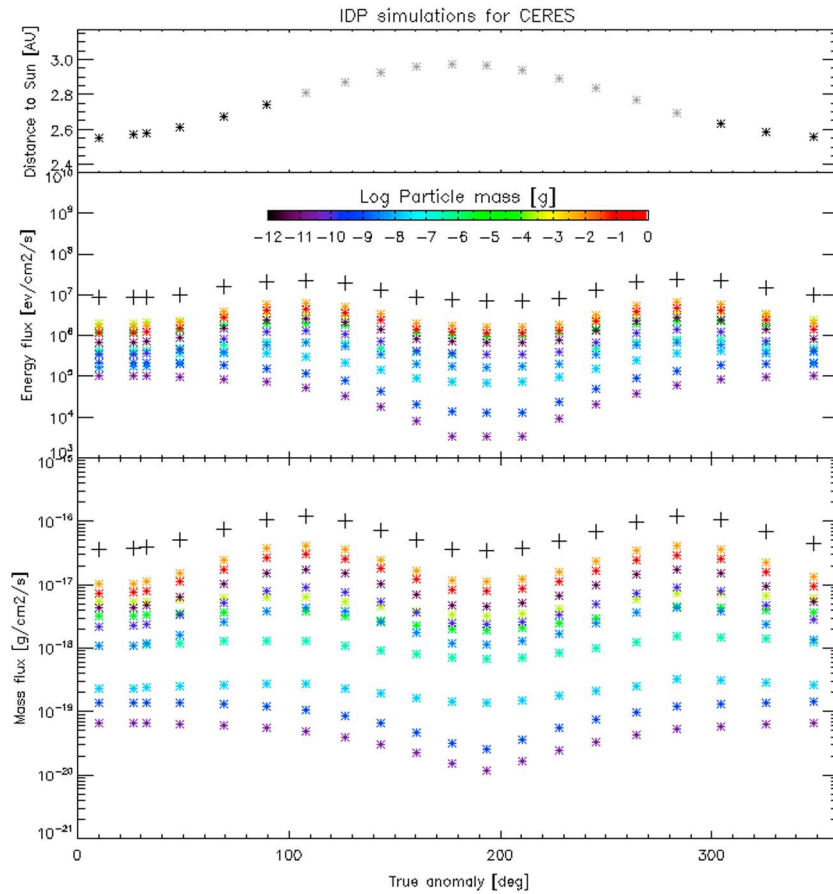


Figure 3. Maximum kinetic energy and mass flux delivered by Jupiter family comets and asteroidal dust along the orbit of Ceres, as function of the body true anomaly. The distance to the Sun is plotted in the upper panel; the kinetic energy and mass flux are plotted in the middle and lower panels, respectively. The upper panel shows the body distance to the Sun, with the black (gray) symbols indicating the northern (southern) latitudes of the orbit. The different colors stand for the different dust mass bins (from 10^{-12} to 1 g) for which the simulations have been performed. The black crosses in the middle and lower panel indicate the total maximum kinetic energy and total mass flux, respectively. IDP = interplanetary dust population.

also Brunetto et al., 2015), the unit of kinetic energy flux is given in $[\text{ev}\cdot\text{cm}^{-2}\cdot\text{s}^{-1}]$. An example of the mass flux and kinetic energy flux computations is shown for Ceres on Figure 3. The corresponding figures for each individual asteroid can be found in Appendix A. A high level summary of the computations is provided in Table 3. For each asteroid, we have indicated the minimum and maximum value of the total mass and kinetic energy flux along the body's orbit.

4.2.1. ISD Impactors

The computation of the ISD grains impact velocities on Ceres surfaces as function of the asteroid's true anomaly is shown on Figure 4. As explained in section 3.1, our modeling of the ISD grain dynamics within the solar system is driven by the β factor. Because the relationship between β and the grain mass depends on grain constitutive models (Kimura et al., 2003), we use different values of β as input to our simulations rather than the mass of the grains. Practically, we run for each asteroid simulations for $\beta = 0.2$, $\beta = 1$, and $\beta = 1.3$. Such values of β cover a wide range of ISD grain types in term of masses and composition (from 10^{-19} to 10^{-12} kg), as detected in situ in the solar system (Altabelli et al., 2016; Grün et al., 1993; Kimura et al., 2003; Mann, 2010). The figures for each asteroid are provided in Appendix A. Important variations of the impact velocity, including discontinuities (e.g., on Figure 4, the blue curve corresponding to $\beta = 0.2$), can be seen depending on the asteroid's position on its orbit. For $\beta > 1$ (e.g., on Figure 4, the yellow curve corresponding to $\beta = 1.3$), there are true anomaly values for which no grain can reach the asteroid. This particular behavior and the impact speed variations can be entirely explained by the strong anisotropy of the ISD stream, the strength of the

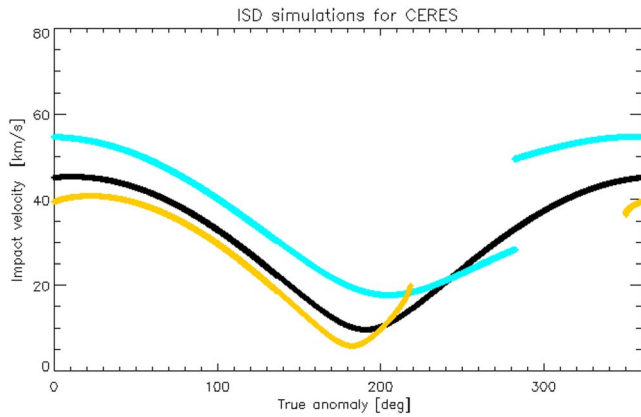


Figure 4. Impact velocity of interstellar dust (ISD) grains on Ceres as function of the asteroid’s position on its orbit, parameterized by the true anomaly. The different line colors correspond to different β values. Black stands for $\beta = 1$, blue for $\beta = 0.2$, and yellow for $\beta = 1.3$. The gap in true anomaly observed for the yellow curve corresponds to the ISD exclusion zone (see text), while the discontinuity in impact speed for the blue curve is due to the passage of Ceres “behind” the Sun, with respect to the ISD stream (see text).

solar radiation pressure, and the position of the asteroid on its orbit with respect to the Sun, as shown on Figure 5.

When $\beta < 1$, the trajectory of ISD grains is an hyperbola with the Sun as focus, with the combination of radiation pressure and gravity resulting in a net attractive radial force. The ISD grains, albeit slower than in the pure gravitative case ($\beta = 0$), can always reach any position of Ceres on its orbit. The impact velocity of ISD grains with $\beta < 1$ is modulated by the relative motion of Ceres to the ISD stream. The apparent discontinuities in impact speed (e.g., at true anomaly $\approx 280^\circ$ on the blue curve of Figure 4) is due to the passage of Ceres behind the Sun, with respect to the ISD stream, and to the convention in our numerical code to take the ISD interception trajectory located on the same side of the Sun than the intercepting body. In the case where $\beta > 1$, however, so-called exclusion zones form behind the Sun (as seen from the ISD downstream direction), where ISD grains cannot penetrate. The boundaries of those exclusion zones are determined by the β value (see Figure 5). The apparent discontinuities of the impact velocities of ISD grains with $\beta = 1.3$ on Figure 4 is explained by the crossing of Ceres of the corresponding boundaries.

We summarize in Table 4 some results from the simulations performed for each asteroid. For the three β values, we indicate the minimum and maximum impact speed in [km/s] expected from the asteroid apex

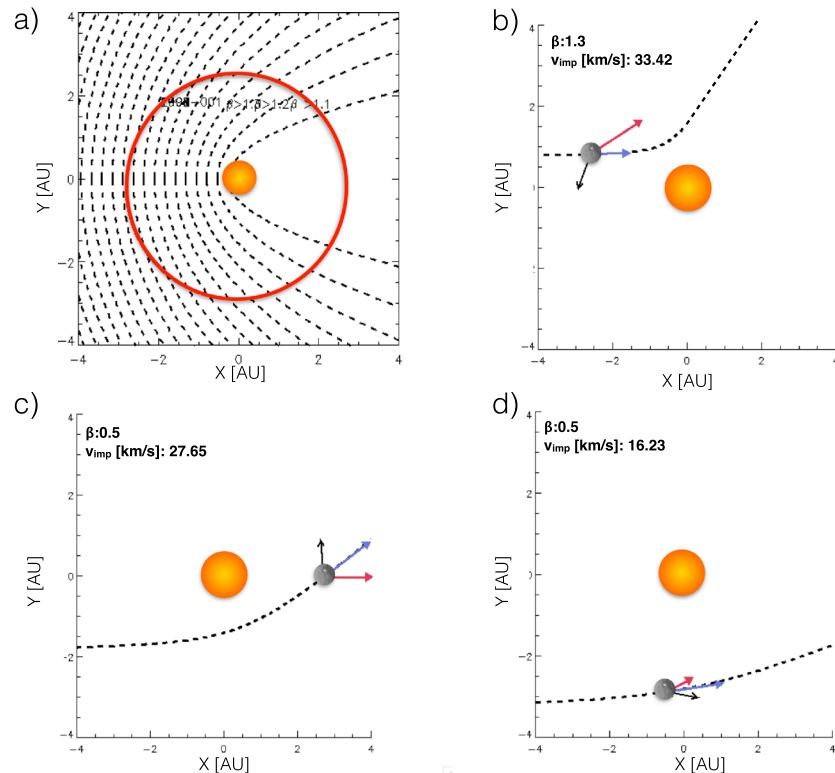


Figure 5. The trajectory of Ceres is plotted (plain line) in an inertial frame on panel a), centered on the Sun, with the +X axis corresponding to the downstream interstellar dust (ISD) direction in the ecliptic frame, and +Z (toward the reader), being the orthogonal component of the ecliptic north direction on +X. +Y completes the right-handed frame. The dashed lines indicate the boundaries of the exclusion zones carved by the solar radiation pressure, whose boundaries depend on the grain β values. The panels (b–d) show in the same frame the hyperbolic trajectories of ISD particles impacting Ceres, for different values of the β parameter. The blue and black vectors indicate, respectively, the heliocentric velocity of Ceres and of the ISD particle, and the red vector represents the impact velocity vector of the dust grain on Ceres.

Table 4

Summary of the ISD Impact Speed and Kinetic Energy Flux Ranges Along the Orbit of the Different Asteroids for Different Values of the Solar Radiation Pressure-to-Gravity Ratio (β)

	$\beta = 0.2$		$\beta = 1$		$\beta = 1.3$	
	V min-max (km/s)	Ek min-max ($\text{eV}\cdot\text{cm}^{-2}\cdot\text{s}^{-1}$)	V min-max (km/s)	Ek min-max ($\text{eV}\cdot\text{cm}^{-2}\cdot\text{s}^{-1}$)	V min-max (km/s)	Ek min-max ($\text{eV}\cdot\text{cm}^{-2}\cdot\text{s}^{-1}$)
EROS	7.3 - 55.3	8.3E+01 - 4.7E+03	18.0 - 74.1	3.9E+03 - 6.6E+05	0.0 - 43.3	0.0E+00 - 4.8E+02
HUNGARIA	8.0 - 45.8	1.0E+02 - 3.2E+03	18.1 - 56.6	3.9E+03 - 3.8E+05	0.0 - 40.5	0.0E+00 - 4.2E+02
VESTA	6.6 - 45.5	6.8E+01 - 3.2E+03	16.8 - 54.8	3.4E+03 - 3.6E+05	0.0 - 40.9	0.0E+00 - 4.3E+02
LUTETIA	4.1 - 42.3	2.6E+01 - 2.8E+03	15.1 - 50.5	2.7E+03 - 3.1E+05	0.0 - 38.5	0.0E+00 - 3.8E+02
PHOCAEA	4.7 - 42.2	3.4E+01 - 2.7E+03	16.8 - 50.1	3.4E+03 - 3.0E+05	0.0 - 38.4	0.0E+00 - 3.8E+02
HC82	19.9 - 82.9	6.1E+02 - 1.1E+04	25.4 - 117.6	7.7E+03 - 1.7E+06	0.0 - 48.0	0.0E+00 - 5.9E+02
ASTRAEA	10.4 - 48.2	1.7E+02 - 3.6E+03	18.0 - 59.4	3.9E+03 - 4.2E+05	0.0 - 42.5	0.0E+00 - 4.6E+02
GANYMED	9.4 - 36.0	1.4E+02 - 2.0E+03	16.8 - 51.4	3.4E+03 - 3.2E+05	0.0 - 33.1	0.0E+00 - 2.8E+02
EUNOMIA	7.0 - 42.0	7.5E+01 - 2.7E+03	15.4 - 51.9	2.8E+03 - 3.2E+05	0.0 - 38.0	0.0E+00 - 3.7E+02
PALLAS	14.9 - 46.2	3.4E+02 - 3.3E+03	21.4 - 58.5	5.5E+03 - 4.1E+05	0.0 - 40.7	0.0E+00 - 4.2E+02
CERES	9.5 - 45.3	1.4E+02 - 3.2E+03	17.6 - 54.6	3.7E+03 - 3.6E+05	0.0 - 40.8	0.0E+00 - 4.3E+02
KORONIS	8.4 - 43.3	1.1E+02 - 2.9E+03	16.5 - 51.9	3.3E+03 - 3.2E+05	0.0 - 39.4	0.0E+00 - 4.0E+02
EOS	7.2 - 41.5	8.1E+01 - 2.7E+03	15.8 - 48.6	3.0E+03 - 2.8E+05	0.0 - 38.2	0.0E+00 - 3.7E+02
THEMIS	11.2 - 44.9	1.9E+02 - 3.1E+03	17.9 - 53.6	3.8E+03 - 3.4E+05	0.0 - 40.8	0.0E+00 - 4.3E+02
HYGIEA	10.1 - 43.6	1.6E+02 - 2.9E+03	17.6 - 51.0	3.7E+03 - 3.1E+05	0.0 - 40.1	0.0E+00 - 4.1E+02
ALAUDA	10.9 - 42.2	1.8E+02 - 2.7E+03	17.9 - 49.4	3.8E+03 - 2.9E+05	0.0 - 38.7	0.0E+00 - 3.8E+02
GRIQUA	6.1 - 38.8	5.8E+01 - 2.3E+03	13.8 - 51.0	2.3E+03 - 3.1E+05	0.0 - 35.4	0.0E+00 - 3.2E+02
SYLVIA	8.7 - 40.5	1.2E+02 - 2.5E+03	16.5 - 47.1	3.3E+03 - 2.7E+05	0.0 - 37.6	0.0E+00 - 3.6E+02
HILDA	10.6 - 40.8	1.7E+02 - 2.6E+03	17.3 - 46.5	3.6E+03 - 2.6E+05	0.0 - 38.2	0.0E+00 - 3.7E+02

direction along its orbit. Zero impact velocities for $\beta = 1.3$ indicate that there are parts of the orbit where the corresponding ISD grains cannot reach the asteroid, as can be seen on the plot for the relevant asteroid on Figures A20-A38. Indicative minimum and maximum kinetic energy fluxes along the orbit are also provided (in [$\text{eV}\cdot\text{cm}^{-2}\cdot\text{s}^{-1}$])—but those values must be considered with caution, because the mass an ISD impactor associated to a given β value depends on an ISD grain constitutive model. In those models, there are generally two mass values corresponding to one β value (see, e.g., Figure 2 of Kimura et al., 2003). In this work, for the purpose of supporting space weathering studies, we report the kinetic energy flux in Table 4 derived from the higher mass value solution, because, for the same β value (and hence impact velocity), large grains will deliver more kinetic energy. For each β value we used the upper solution for the mass of the silicate ISD grain models consistent with recent Cassini-CDA measurements (Altobelli et al., 2016, their Figure 3). The corresponding grains mass ranges are, roughly, $M > 10^{-14}$ kg for $\beta \leq 0.2$, 10^{-16} kg $< M < 10^{-14}$ kg for $0.2 < \beta < 1$ and $5\cdot 10^{-17}$ kg $< M < 10^{-16}$ kg for $\beta > 1$. Finally, to provide an upper value for the kinetic energy flux of impactors described by their β value, we have done the following simplification, which we believe is sufficient for the purpose of this study: Considering the ISD mass distribution and flux values reported by (Krüger et al., 2015), we apply a flux of $5\cdot 10^{-5}\text{m}^{-2}/\text{s}$ to the particles with $\beta = 1.3$, $10^{-5}\text{m}^{-2}/\text{s}$ to the particles with $\beta = 1$ and $10^{-6}\text{m}^{-2}/\text{s}$ to the particles with $\beta = 0.2$.

5. Discussion

We have performed simulations of interstellar and interplanetary dust (from JFCs and asteroid sources) impacts on asteroids representative of different dynamical groups in order to quantify the mass-dependent impact speeds, the relative abundance of different impactor populations as defined by the IMEM model, and the total mass and kinetic energy flux received by the asteroids. The simulations have been performed for all bodies such as to cover a full orbit around the Sun. For each asteroid, and each position on its orbit, the maximum values from all possible radiant directions have been chosen. We discuss the model limitations for our study, before focusing on our results.

5.1. Model Limitations

Dust particles released by highly eccentric and highly inclined comets, such as Halley-type comets (HTCs) or Oort Cloud-type comets (OCCs), are not included in the current version of the IMEM model and therefore not considered for detailed flux and impact velocity computations. Those cometary sources can produce dust populations on retrograde orbits (heliocentric inclination larger than 90°). Retrograde populations released by HTCs were shown to contribute by less than 10% to the zodiacal cloud brightness, using different models and calibration methods (Nesvorný et al., 2010; Pokorný et al., 2014). Despite the smaller abundance of dust from HTCs compared to the abundance of dust populations released by JFCs, highly inclined HTC grains will impact prograde asteroids with higher impact speed and are therefore efficient at delivering kinetic energy to the asteroids surfaces. Recent work has demonstrated that retrograde IDPs of HTC or OCC origin must be the dominant producers of ejectas on the lunar surface and on the surface of asteroids near 1 AU (Szalay & Horányi, 2015, 2016). Owing to the high speed and retrograde orbits of those particles, retrograde particles will deposit their energy onto the asteroids surfaces facing the apex direction.

The inclusion of retrograde dust populations (from HTCs or OCCs) in numerical models like IMEM has suffered in the past decades from the relatively low statistics of observations to support the models calibration (e.g., the lack of direct in situ characterization of retrograde populations by dust instruments on-board spacecraft in the inner solar system; Altobelli et al., 2007). While a next version of the ESA micrometeoroid model (IMEM2), considering HTCs sources, is currently being developed, preliminary results show that the impact speed of HTC-type dust can reach up to three times the values of JFC particles, for a total HTC dust abundance being only 1% of the JFCs dust abundance in the inner solar system. This value is significantly lower than the 10% abundance at 1 AU reported by Nesvorný et al. (2010)—confirmed by Pokorný et al. (2014) to be an upper limit value. For our purpose of evaluating the impact speed and kinetic energy flux range on the surface of asteroids, we consider the 1% and 10% values to be the lower (upper) limit of HTC abundance in the inner solar system, and we assume an upper limit of 3 times the JFC impact velocity values for all asteroids studied in this work (except, of course, for the retrograde asteroid 2009-HC82). Furthermore, if we assume the mass distribution of the grains released by HTCs to be the same than those of JFCs, HTC dust will deliver between 3% and 30% of the JFC dust contribution in terms of particle and mass flux, and between 0.3 and 3 times the JFC dust kinetic energy. The dominance of the apex source reported by Szalay and Horányi (2015) suggests that the retrograde dust contribution must be in fact on the higher side compared to the contribution by prograde dust, but for the purpose of this paper, a conservative estimate of the retrograde dust impact characteristics can be simply obtained by applying those factors to the JFC dust simulation results discussed in the next paragraphs.

5.2. Simulation Results

For a given dust population, the variability of the impact speed and fluxes (mass and kinetic energy) appears, as expected, to depend primarily on the asteroids heliocentric orbital elements (semimajor axis, inclination, and eccentricity). For all asteroids considered in this work, the highest impact speeds are reached by the JFC dust populations (CC or CPR), ranging between 15 and 30 km/s for prograde asteroids (i.e., having an inclination lower than 90° with respect to the ecliptic plane). This finding is consistent with the fact that grains from JFCs are released by their parent bodies on orbits with larger eccentricities and inclinations values compared to the eccentricities and inclinations of the orbits of the impacted asteroids, resulting in high relative velocities. Dust populations released by asteroidal sources, in turn, impact prograde asteroids with significantly lower impact speeds, ranging between 2 to 10 km/s for asteroids with low to moderate eccentricities and inclinations. This is qualitatively consistent with the fact that large grains produced by fragmentation of larger bodies within the main belt (AC type in our modeling) will yield the lowest impact speed as they tend to remain on orbital elements close to those of their parent body and will therefore keep low relative speeds with respect to other main belt objects. In turn, asteroids with either large eccentricities or inclinations, or both, will tend to be impacted by IDPs of cometary or asteroidal origin at similar impact speeds, primarily driven by the difference of the asteroid's own orbital elements (and hence higher relative velocity) compared to those of the bulk of the different dust populations. This effect is particularly pronounced for the retrograde, highly eccentric asteroid 2009-HC82, for which all dust populations appear to have nearly the same impact speed along the asteroid's orbit (see relevant plot in Appendix A1).

For all simulated asteroids, the relative contribution of dust of cometary (JFCs) origin (in terms of particle flux) is larger than the asteroidal one by about 1 order of magnitude when the asteroid is located within the ecliptic plane (near its ascending and descending orbital nodes—those regions correspond to the transition between the thick and thin lines on the plots in Appendix A1, upper plots of Figures A1-A19). The flux of cometary impactors can even exceed by multiple orders of magnitude the asteroidal flux for asteroids with inclined orbits, when the body is located outside of the ecliptic plane (see, e.g., in Figure A10, left panel, the strong reduction of the asteroidal flux for Pallas when located at 100–200° or 300–360° true anomaly, corresponding to, respectively, high northern and southern ecliptic latitudes). The higher cometary particle flux in the two main mass range domains of the model (see section 3) implies overall higher mass fluxes of cometary dust impacting the asteroids surface than asteroidal dust. This conclusion holds for all main belt and NEO asteroids studied in this work. As we have selected bodies with orbital elements covering a wide range of observed asteroids, the cometary dust contribution is very likely to dominate the mass influx onto the surface of all bodies of the inner solar system. This point would be in agreement with Nesvorný et al. (2010) who had concluded that dust from JFCs contribute most to the mass influx of micrometeoroids at the Earth.

The contribution of ISD has been evaluated for all asteroids along their orbits. Due to the strong anisotropy of the ISD flux, there are strong variations of the impact velocities as function of the true anomaly of the impacted body. Grains small enough such that the solar radiation pressure exceeds the solar gravity (grains with $\beta > 1$) are not able to reach the asteroid during some part of its orbit (see, e.g., in Figure 4, yellow curve, no grain with $\beta = 1.3$ can reach Ceres when located at 220–350° true anomaly). For some combinations of β and true anomaly, ISD impactors can yield the highest impact velocity values for all asteroids, exceeding the highest impact speed of cometary grains. However, the flux of kinetic energy deposited by ISD grains on the asteroid surfaces is significantly smaller than the one of IDPs, because, on the one hand, the flux of ISD grains in the inner solar system, typically between 10^{-5} and 10^{-4} m²/s (Krüger et al., 2015; Landgraf et al., 2003; Mann, 2010), will be lower than the asteroidal and cometary grain contribution in the low mass regime (mass lower than 10^{-6} g; see section 3) and, on the other hand, the most abundant ISD grains have orders of magnitude less mass (typically, around 10^{-13} g) than the IDPs contributing most to the kinetic energy flux (typically around 10^{-4} – 10^{-3} g; see Figure A11, and all right panels on the plots in Appendix A1). As a result the upper limit for kinetic energy deposition by ISD does not exceed a few 10^5 eV·cm²·s⁻¹ for most asteroids (Table 4), while we find a flux of IDP kinetic energy in a range of 10^6 – 10^8 eV·cm²·s⁻¹ (Table 3), with only the retrograde NEO asteroid 2009-HC82 impacted by a maximum kinetic energy flux up to almost 10^{11} eV·cm²·s⁻¹.

Considering the left panels of the plots in Appendix A1, showing the impact energy per IDP mass bin, we observe that the highest impact energy is not necessarily deposited by the largest grain size, on the one hand, because, according to our simulations, the larger grains tend to have the lowest impact velocities on the main belt asteroids, and, on the other hand, because the grain size abundance (volume number density) tends to naturally follow a power law distribution with negative index, both for cometary and asteroidal grains (Grün et al., 1985). As a result, there is a mass range where the combination of impact velocity, mass, and particle number flux yields the highest kinetic energy flux. For asteroids in the inner main belt (low semimajor axis values), the maximum energy is deposited by grains in the 10^{-4} – 10^{-3} g mass range, while for asteroids located further away, larger grains (10^{-3} – 10^{-2} g) appear to deliver most of the energy.

In addition, Figure A11 (and all similar plots in Appendix A1) shows that among the large grains bringing most of the kinetic energy, those of cometary origin will largely dominate the overall kinetic energy influx. Indeed, combining the up to about a factor of five higher impact speed values for cometary grains compared to asteroidal grains, and the higher cometary dust impact mass flux (about 2 orders of magnitude larger for most asteroids), the kinetic energy flux deposited by cometary dust will be at least 2,500 times larger than the asteroidal one. This fact, combined with the knowledge gained by the Rosetta mission on cometary dust, allows to better constrain the requirements on laboratory studies reproducing weathering of asteroid surfaces through micrometeoroids. In particular, the type of large cometary dust grains that deposit most of the kinetic energy in our simulations would consist of fractal aggregates with high porosity (Fulle & Blum,

2017). Those aggregates fragment easily (Hornung et al., 2016) and are made of individual compact grains with a bulk density of 800 to 3,000 kg/m³ (Fulle et al., 2015), whose mechanical properties are described in Hilchenbach et al. (2017).

Overall, the upper energy flux deposited by JFC and asteroidal dust (as well as HTC dust) is orders of magnitude lower than the one deposited by agents such as solar photons (from IR to hard X-ray; see Table 1 of Bennett et al., 2013). From the same table we see that the dust energy flux is comparable to the energy flux brought by solar wind heavy ions and electrons or galactic cosmic rays, while remaining 1 or 2 orders of magnitude lower than the proton energy flux (depending on solar activity). We note that the solar wind carries another space weathering agent potentially effective at depositing kinetic energy on asteroids' surfaces: the so-called nanodust grains, as characterized by the Stereo spacecraft (Juhász & Horányi, 2013). Those grains have their origin near the Sun and have masses between 10⁻²² and 10⁻²⁰ kg, resulting in a high charge-to-mass ratio that makes them behave dynamically like ions carried with the solar wind at very high speeds (reaching up to a few hundreds of km/s near 1 AU). Assuming an upper limit value for their impact velocity on asteroid surfaces of 400 km/s, each nanograins will carry an impact energy ranging from 5.10⁷ to 5.10⁹ eV. Owing to their generation process near the Sun, the flux of those particles will decrease with the heliocentric distance squared, but they may remain an important agent of space weathering of airless bodies in the inner solar system. Because of their very low mass and size, however, impacts of nanodust grains may induce surface alterations more similar to the ones caused by heavy ions, rather than the gardening and melting caused by micrometeoroid impacts.

Considering our simulated dust flux values, the total amount of exogenous material delivered to an asteroid surface appears very small: a typical mass flux value of 10⁻¹⁶ g·cm⁻²·s⁻¹ will yield about only 10⁻³ g/cm² per My, which is in turn the short time scale needed by the solar wind implantation to give its final color to a freshly exposed asteroid surface (Vernazza et al., 2009). Thus, it does not appear plausible, considering the low dust flux, that surface coating by exogenous material deposited by dust grains can compete with solar wind to determine the spectral characteristics of the asteroids surfaces. Furthermore, a dust coating mechanism, with a main cometary dust contribution, cannot account for the diversity of spectral characteristics encountered for the asteroids across the main belt (DeMeo & Carry, 2013, 2014).

In turn, dust impacts are more likely to provide a microscale surface rejuvenation process, by gardening and vaporization of the surface upper layers, exposing material previously hidden from the solar wind irradiation, and therefore counteracting the effect of solar wind implantation. The production of impact ejectas upon micrometeoroid bombardment has been estimated in details for any airless body near 1 AU by Szalay and Horányi (2016). The detailed amount of surface material ejected upon impact of a meteoroid depends on the surface and impactor's composition, impact speed, and impact angle and was shown experimentally to account for up to 1,000 times the impactor's mass for ice and silicate mixtures (Koschny & Grün, 2001). In addition, using the formulae of Ahrens and O'Keefe (1987), Berezhnoy and Klumov (2008) calculated that the amount of vapor released during an (vertical) impact on the surface of Mercury is 10 times the impactor's mass at 20 km/s and 60 times the impactor's mass at 60 km/s. Micrometeoroids impacting the asteroid surface over billions of years are therefore playing a key role in the erosion and gardening of the body's surface, despite their relatively low kinetic energy flux. Finally, hypervelocity dust impacts onto a surface will send shock waves through the asteroid's upper layers, resulting in high-pressure metamorphism of its surface and subsurface material Tschauer et al. (2018).

Whatever the weathering effects of dust impacts on asteroid surfaces may be, Figure 6 shows that all asteroids with a *prograde* orbit should be affected similarly. Indeed, the impact speed and kinetic energy flux range values of the JFC dust grains (the main contributors in our model), as function of the semimajor axis of the selected asteroids, show a large overlap for all asteroids with a *prograde* orbit. While the differences in eccentricities and inclinations result in wider ranges, the impact velocity and flux appear independent of the semimajor axis. This finding suggests that the spectral differences between different *prograde* asteroid families in the inner solar system cannot be directly linked to orbital element dependent variations of the dust bombardment of their surfaces. The situation may be different, however, for the comparatively rare asteroids with retrograde orbits (such as 2009 HC82), for which the much higher dust impact speed and flux may induce a more intense gardening of their surface.

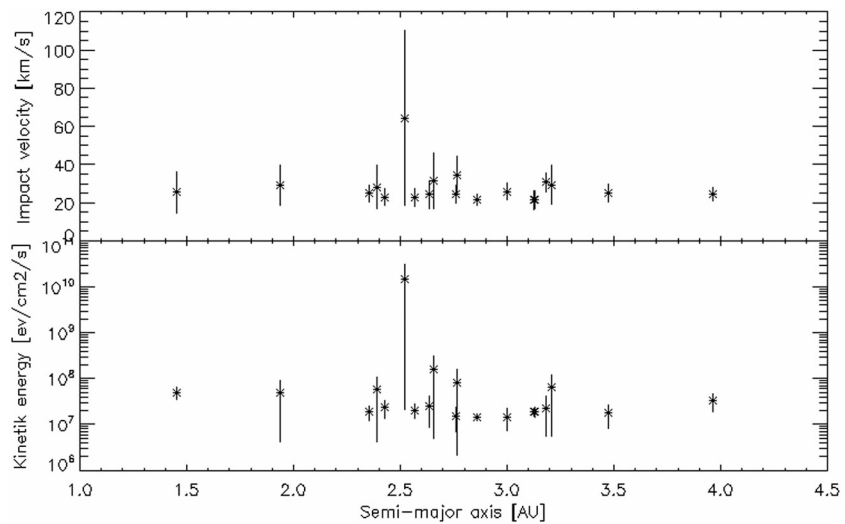


Figure 6. Range values of impact velocity (upper panel) and kinetic energy flux (lower panel), as function of the semimajor axis, for all asteroids selected in this work.

6. Conclusion

Simulating experimentally the effect of micrometeoroid impacts on asteroid surfaces is an important step to understand how dust acts as a space weathering agent to modify the body's surface physical properties. The modeling presented in this work constrained the impact speed and kinetic energy flux regimes to be reproduced in the laboratory to perform impact experiments as close as possible to the conditions that prevail for main belt and near Earth asteroids. The numerical simulations performed in this work were performed using the micrometeoroid environment model (IMEM) developed for ESA to reproduce the contribution of dust from asteroids and JFCs in the inner solar system and a separate ISD model. The contribution of dust from HTCs was evaluated based on preliminary runs of the latest version of IMEM, under development, and by scaling the JFC contribution. The asteroids used for the simulations were chosen such as to represent the diversity of the asteroid dynamical families of the main belt and near Earth. The simulations show the variation of the dust impact speed, dust mass influx, and kinetic energy as function of the position of the asteroids on their orbits. The dust impactors appear to deposit orders of magnitude less energy than solar radiations. While their contribution in terms of energy is comparable to heavy solar wind ions and electrons, the kinetic energy is deposited onto the surface over a much larger cross section and may therefore lead to different alteration processes, related in particular to the dissipation of the energy within the surface material through the formation of an impact plasma and shock waves. We quantified the relative contribution of the dust impactor of interstellar, cometary, and asteroidal origin, showing that large cometary grains dominate the kinetic energy flux. This fact has important implications for constraining future laboratory impact simulations since the properties of large cometary grains have been investigated in details by the Rosetta mission. Overall, we find that the dust bombardment of asteroids with prograde orbits in the inner solar system varies little with the asteroid's orbital elements, suggesting that dust impacts are unlikely to be responsible for the surface spectral trends, although they may counteract by surface gardening the effect of solar wind implementation.

Appendix A: Annex

In this annex we provide figures for each asteroid discussed in this work, summarizing for IDPs and ISD the computations of the dust impact velocity and flux values along the asteroid's trajectory. The flux computations for IDPs include the particle's flux, as well as the mass and kinetic energy flux (see caption of Figure A1 for details). Figures A1–A19 show the computations for IDPs, while Figures A20–A38 show the impact velocity computations for ISD.

A1. Individual Asteroid Simulations for IDPs

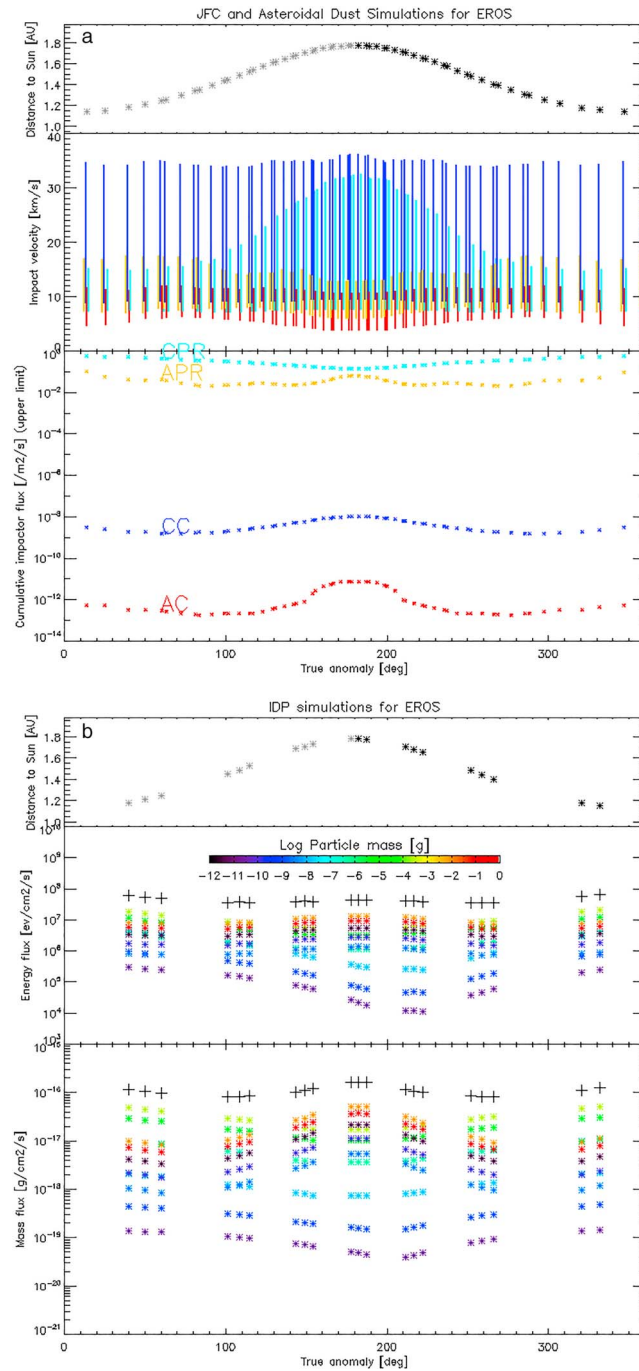


Figure A1. Upper plot: flux and velocity of dust impactors along the asteroid's orbit. Top: distance of the asteroid to the Sun in astronomical units as function of its true anomaly. The gray (black) symbols indicate when the asteroid is located at southern (northern) ecliptic latitude. Middle: impact speed range. Bottom: maximum cumulative particle flux. The red and yellow colors in the middle and lower panels stand for the asteroidal collision (AC) and asteroid Poynting-Robertson (APR) dust populations, and the dark and light blue curves for the cometary comet collision (CC) and comet Poynting-Robertson (CPR) dust populations. Bottom plot: maximum kinetic energy and mass flux delivered by Jupiter family comets (JFCs) and asteroidal dust along the asteroid's orbit, as function of the body true anomaly. The distance to the Sun is plotted in the upper panel; the kinetic energy and mass flux are plotted in the middle and lower panels, respectively. The upper panel shows the body distance to the Sun, with the black (gray) symbols indicating the northern (southern) latitudes of the orbit. The different colors stand for the different dust mass bins (from 10⁻¹² to 1 g) for which the simulations have been performed. The black crosses in the middle and lower panel indicate the total maximum kinetic energy and total mass flux, respectively. IDP = interplanetary dust population.

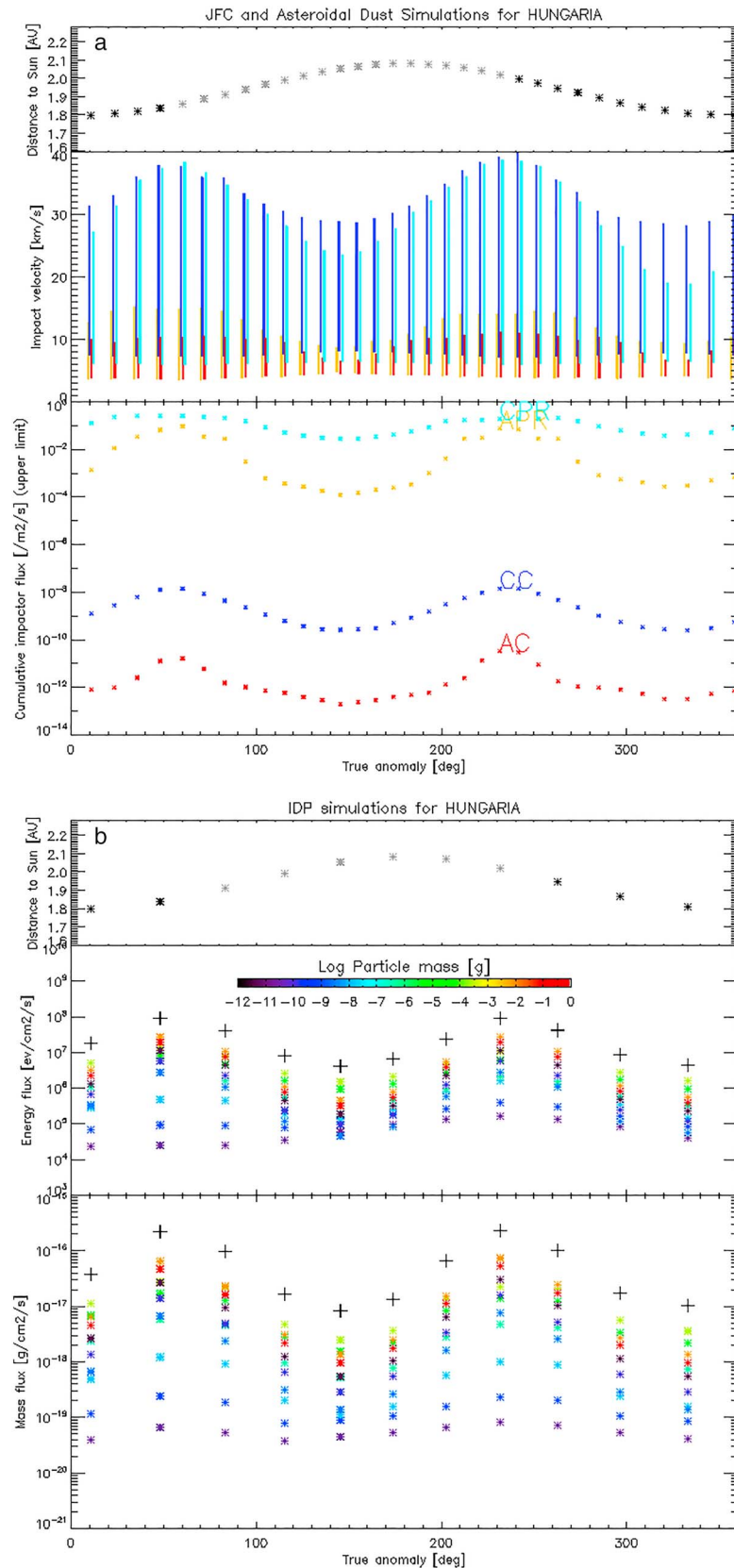


Figure A2. See Figure A1 caption.

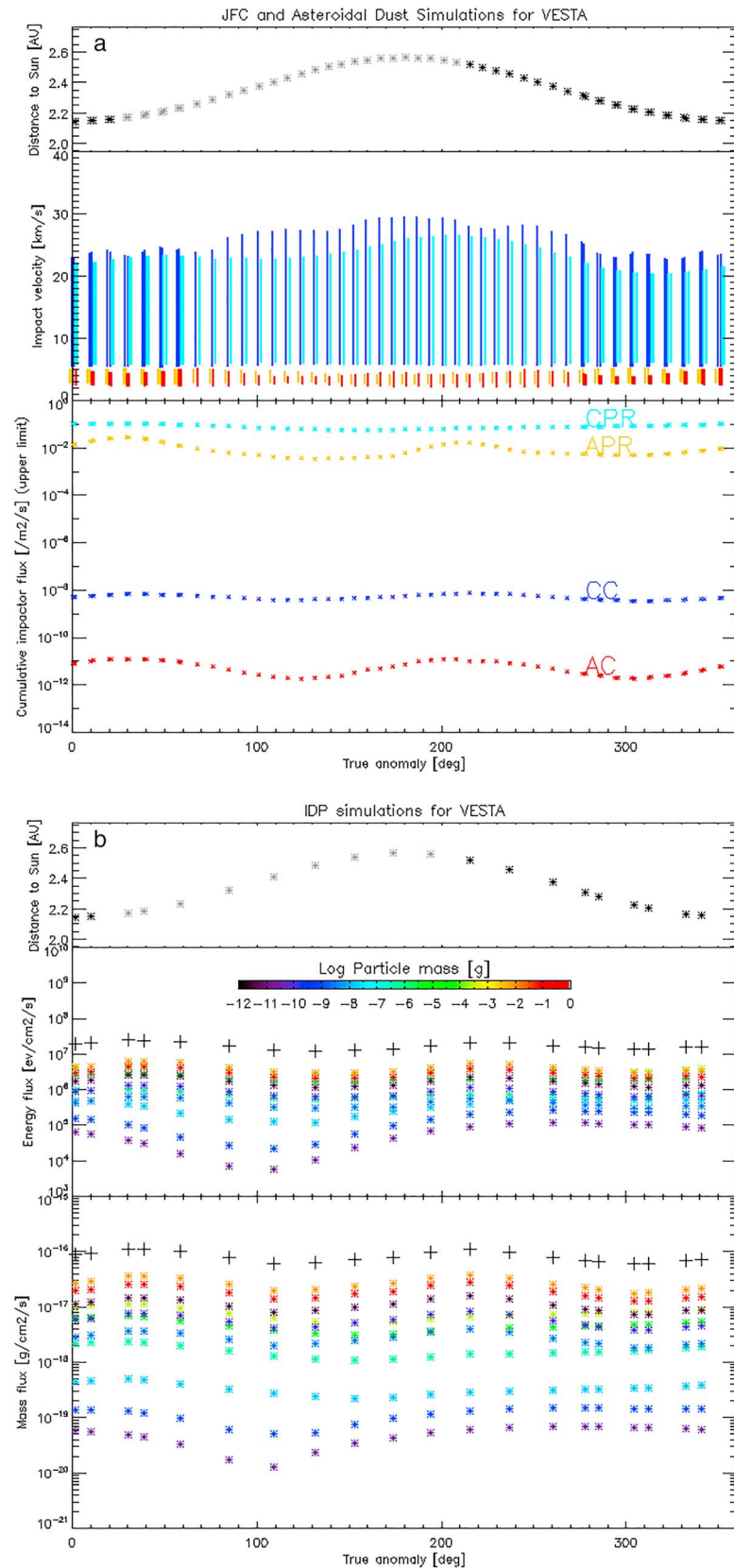


Figure A3. See Figure A1 caption.

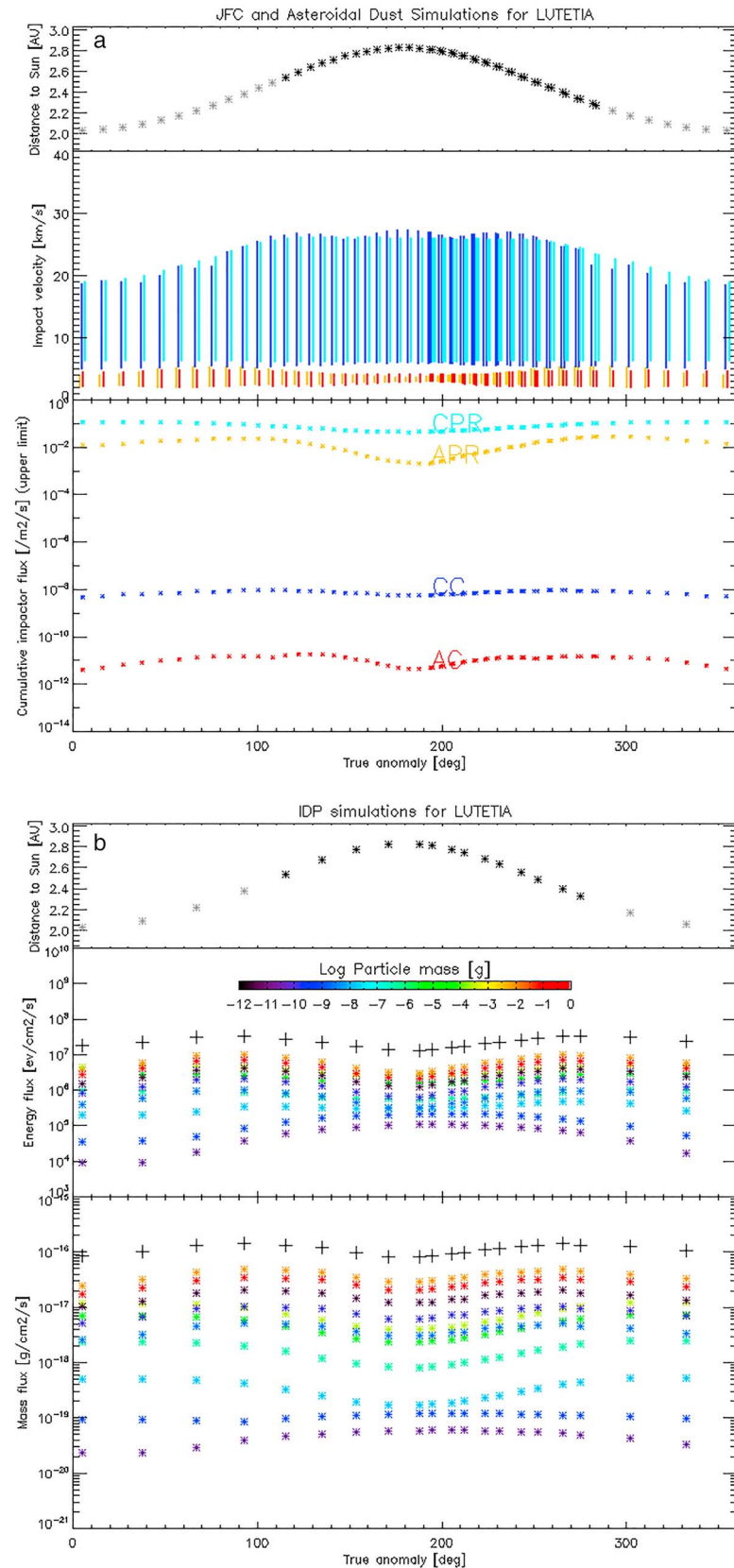


Figure A4. See Figure A1 caption.

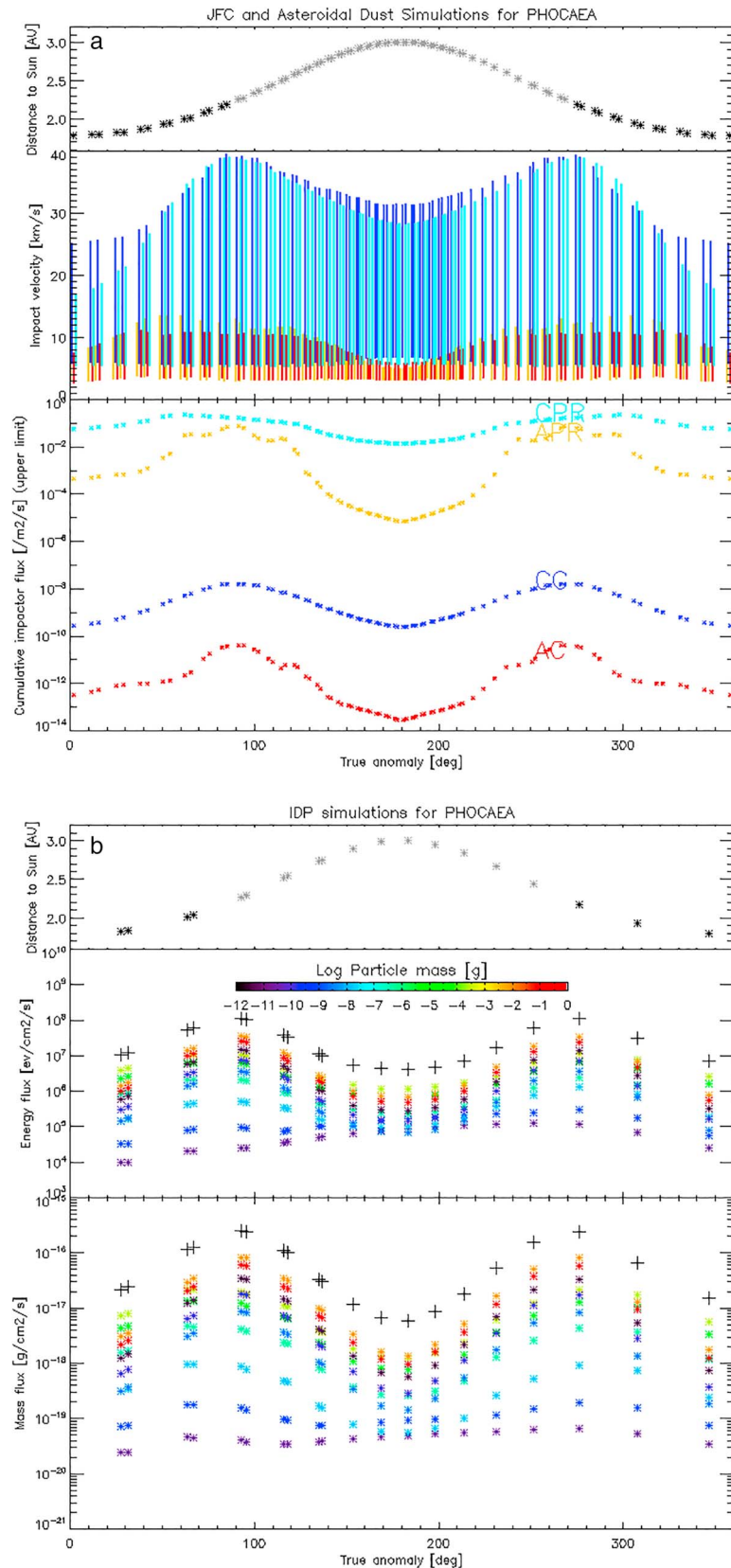


Figure A5. See Figure A1 caption.

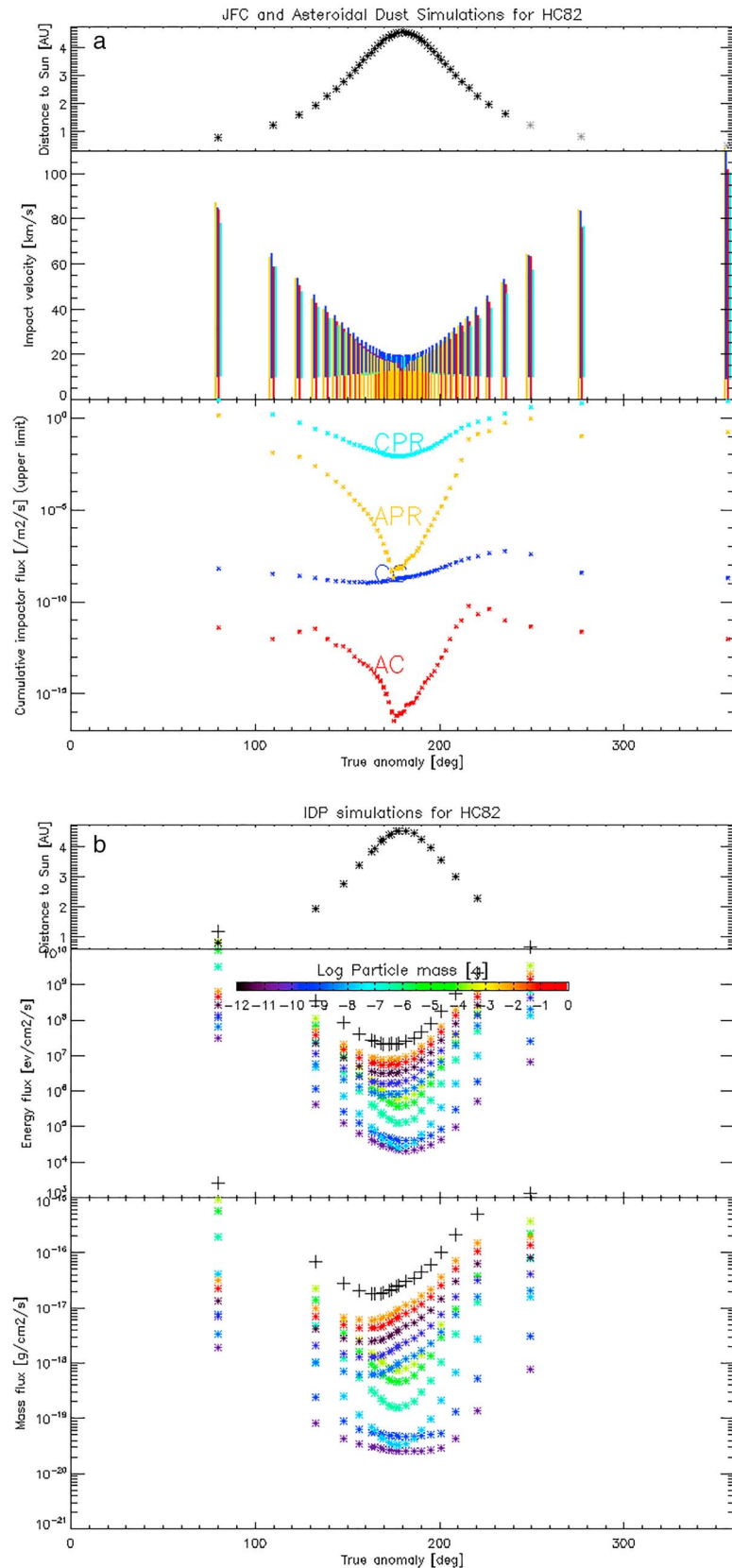


Figure A6. See Figure A1 caption.

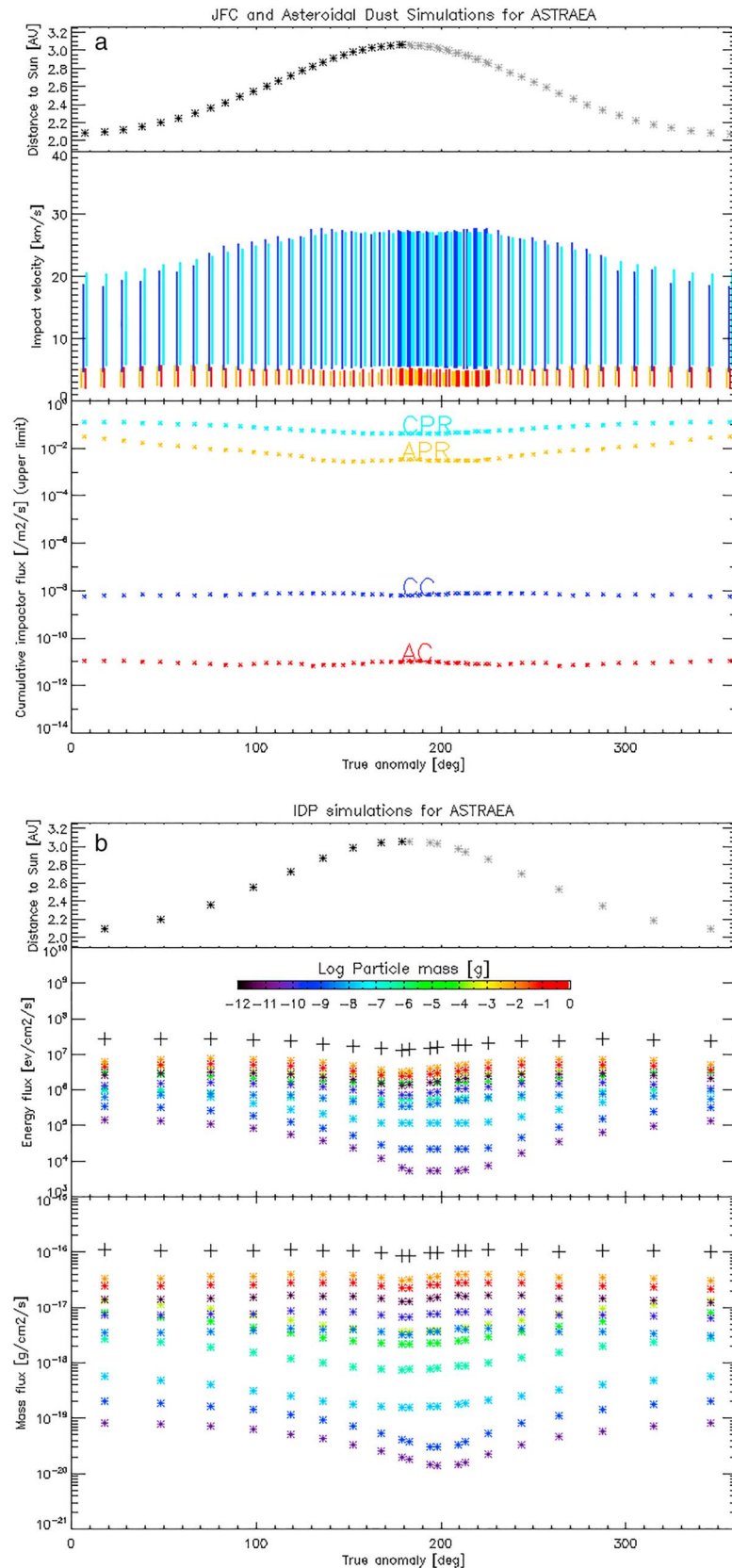


Figure A7. See Figure A1 caption.

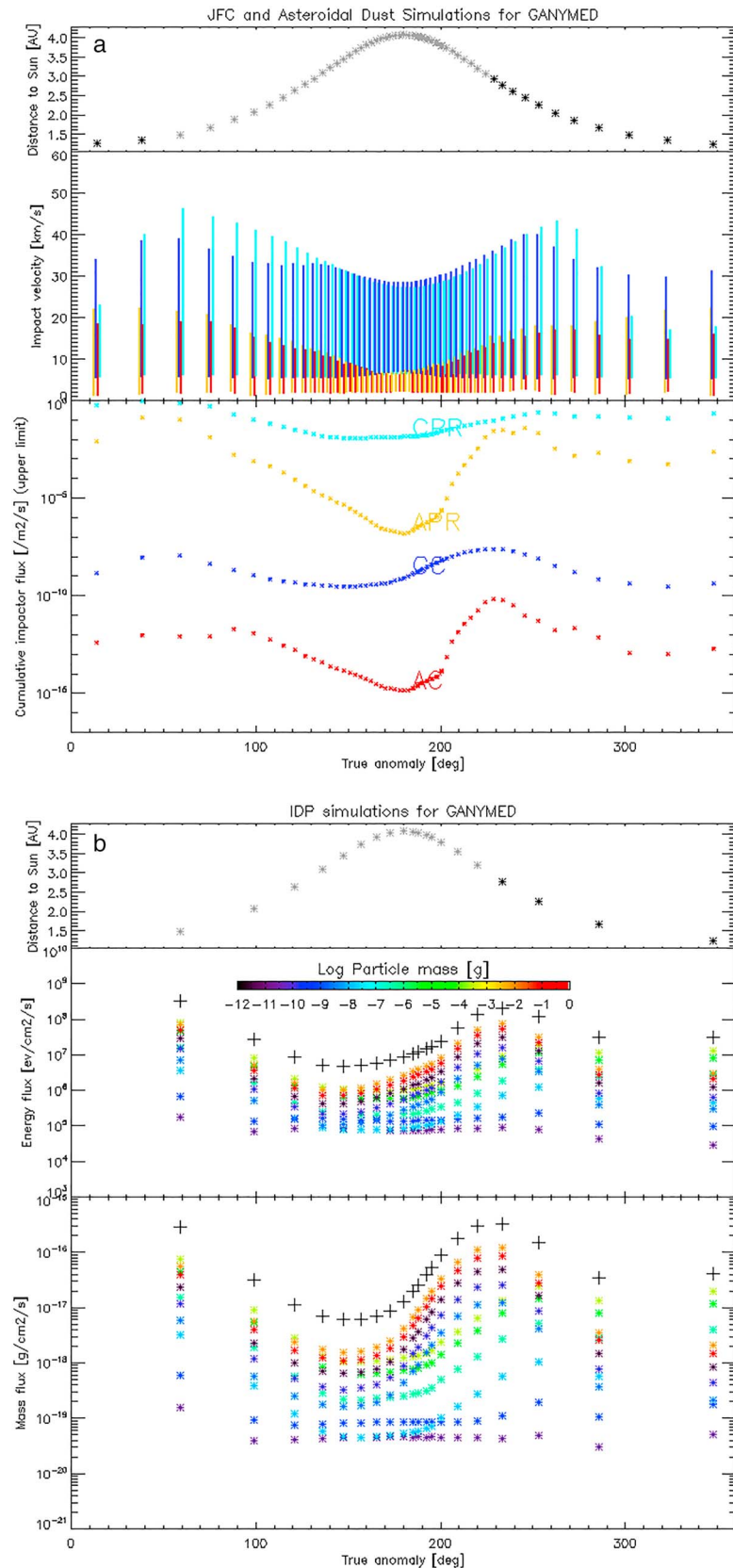


Figure A8. See Figure A1 caption.

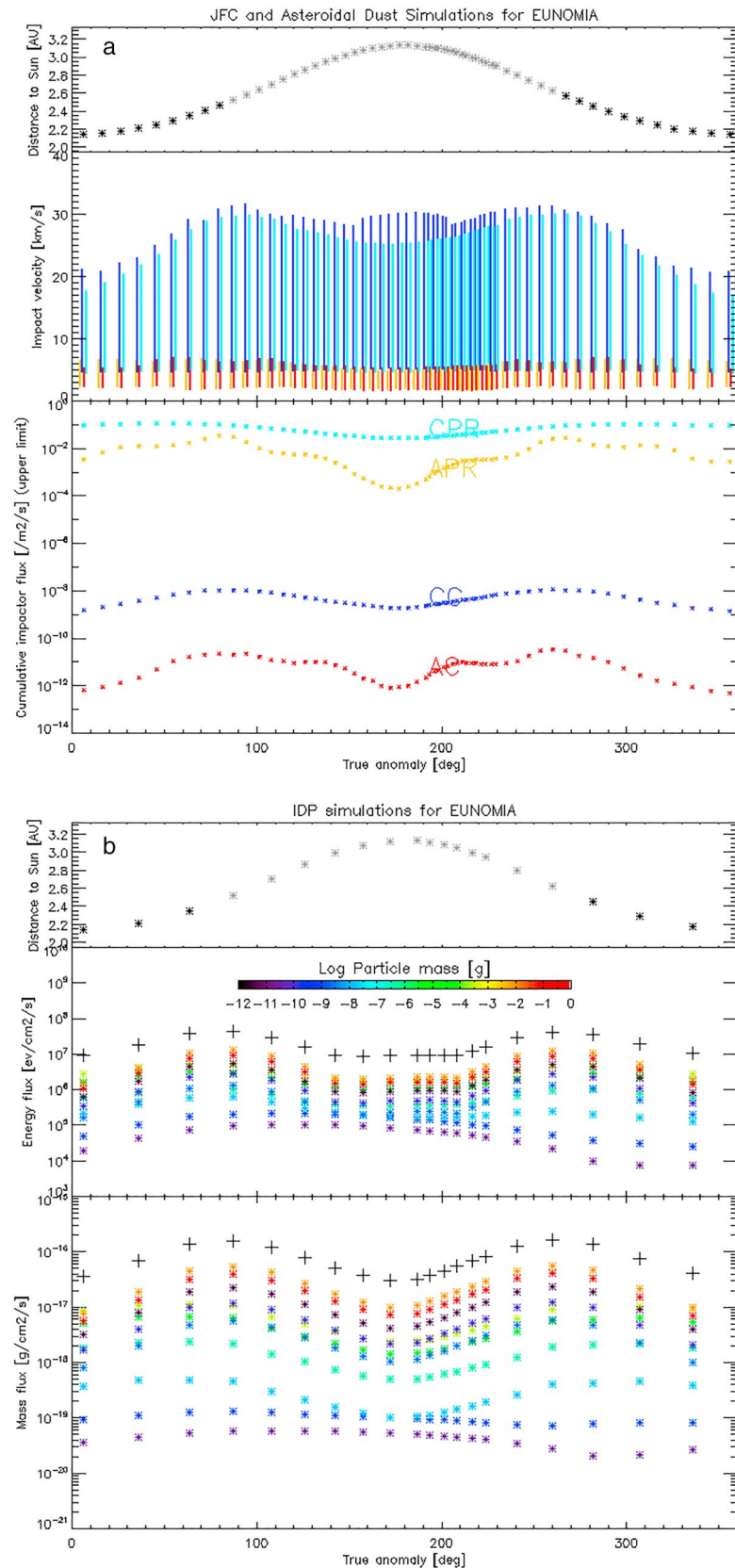


Figure A9. See Figure A1 caption.

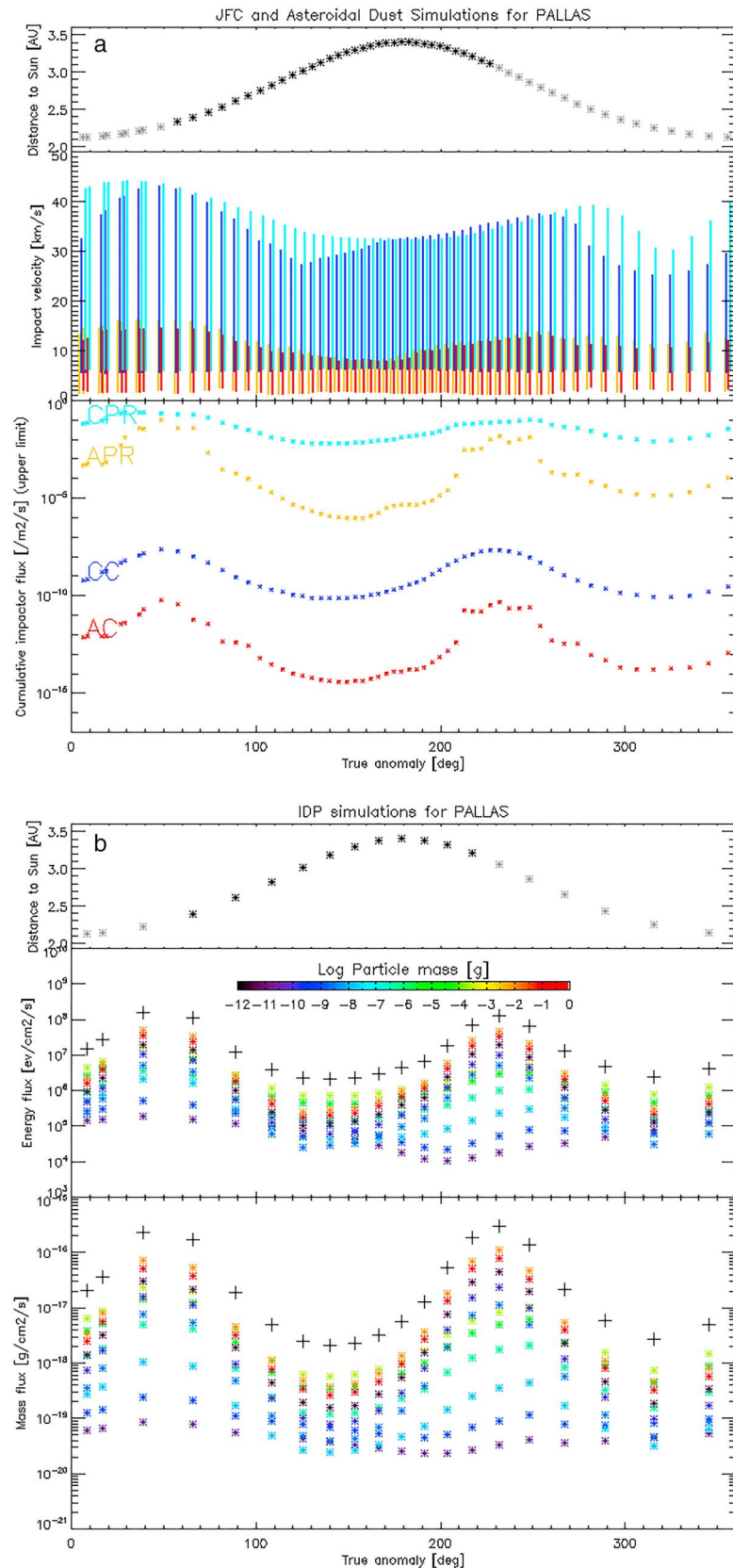


Figure A10. See Figure A1 caption.

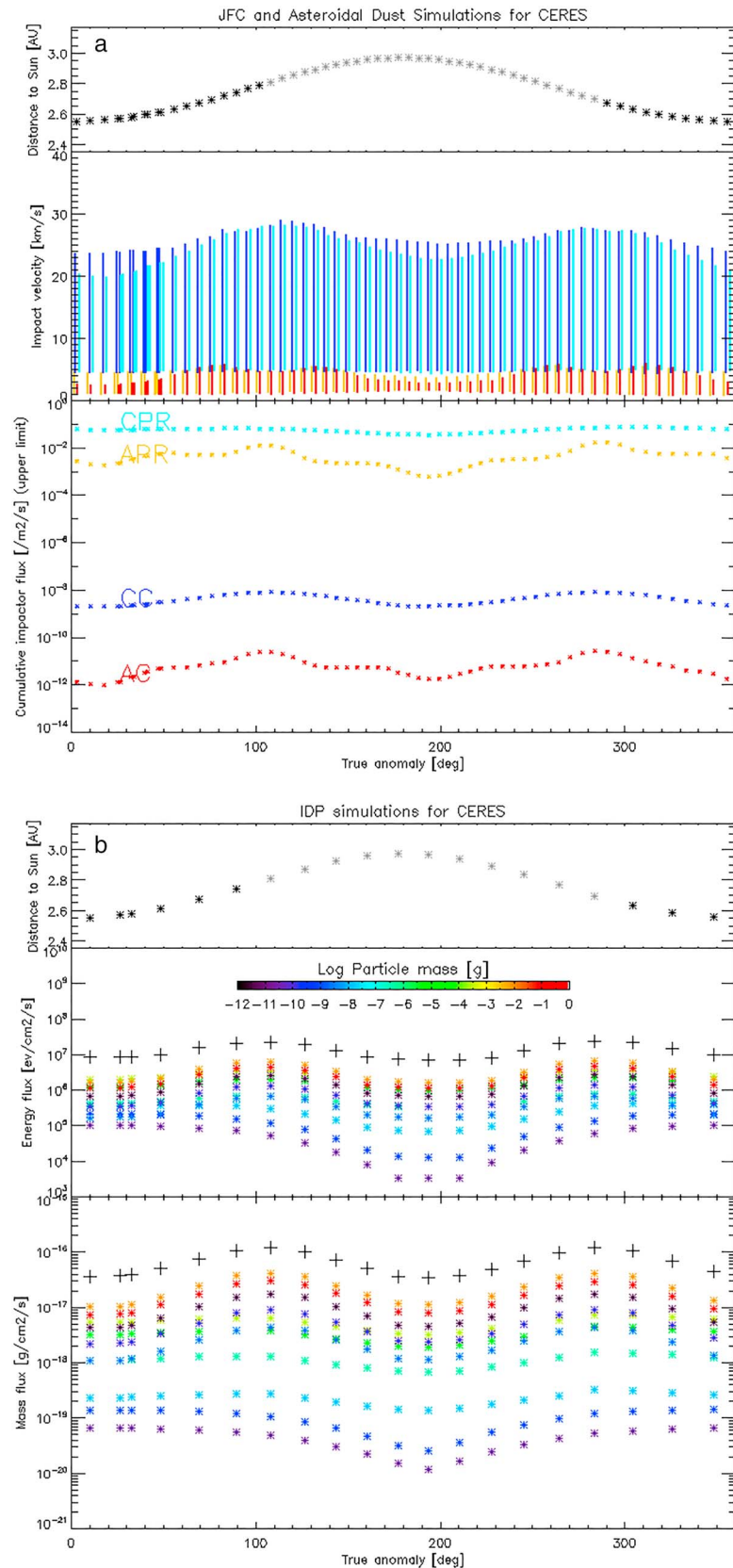


Figure A11. See Figure A1 caption.

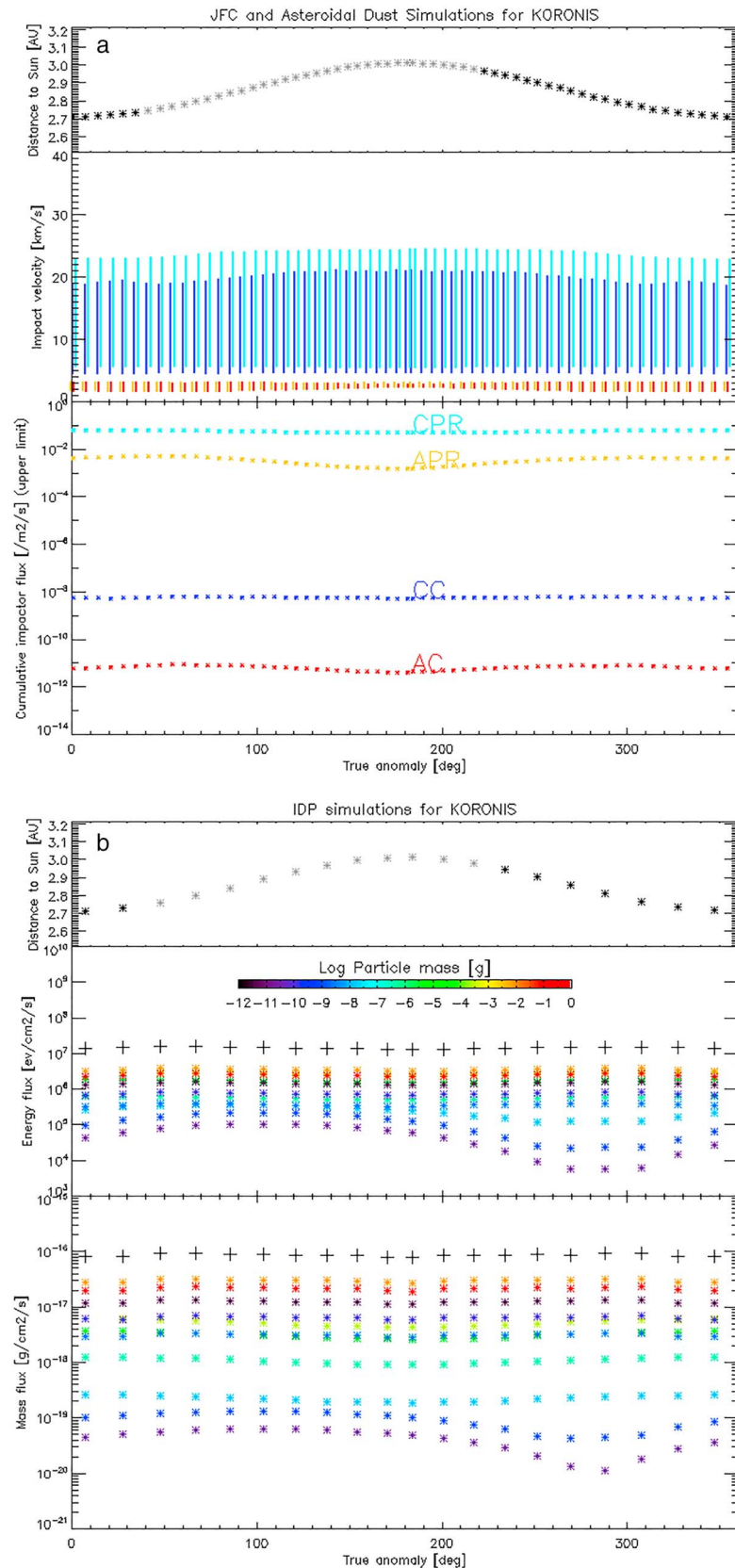


Figure A12. See Figure A1 caption.

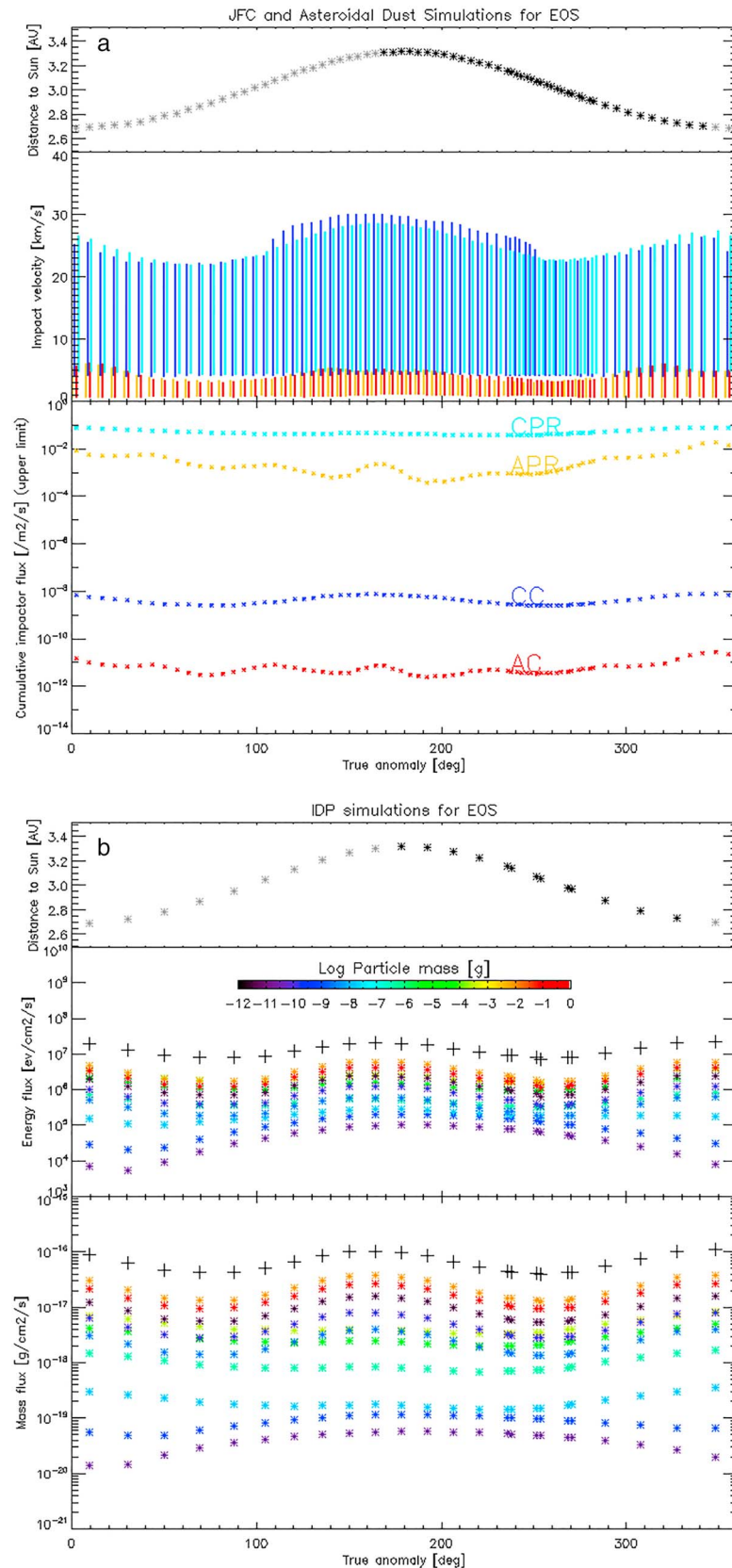


Figure A13. See Figure A1 caption.

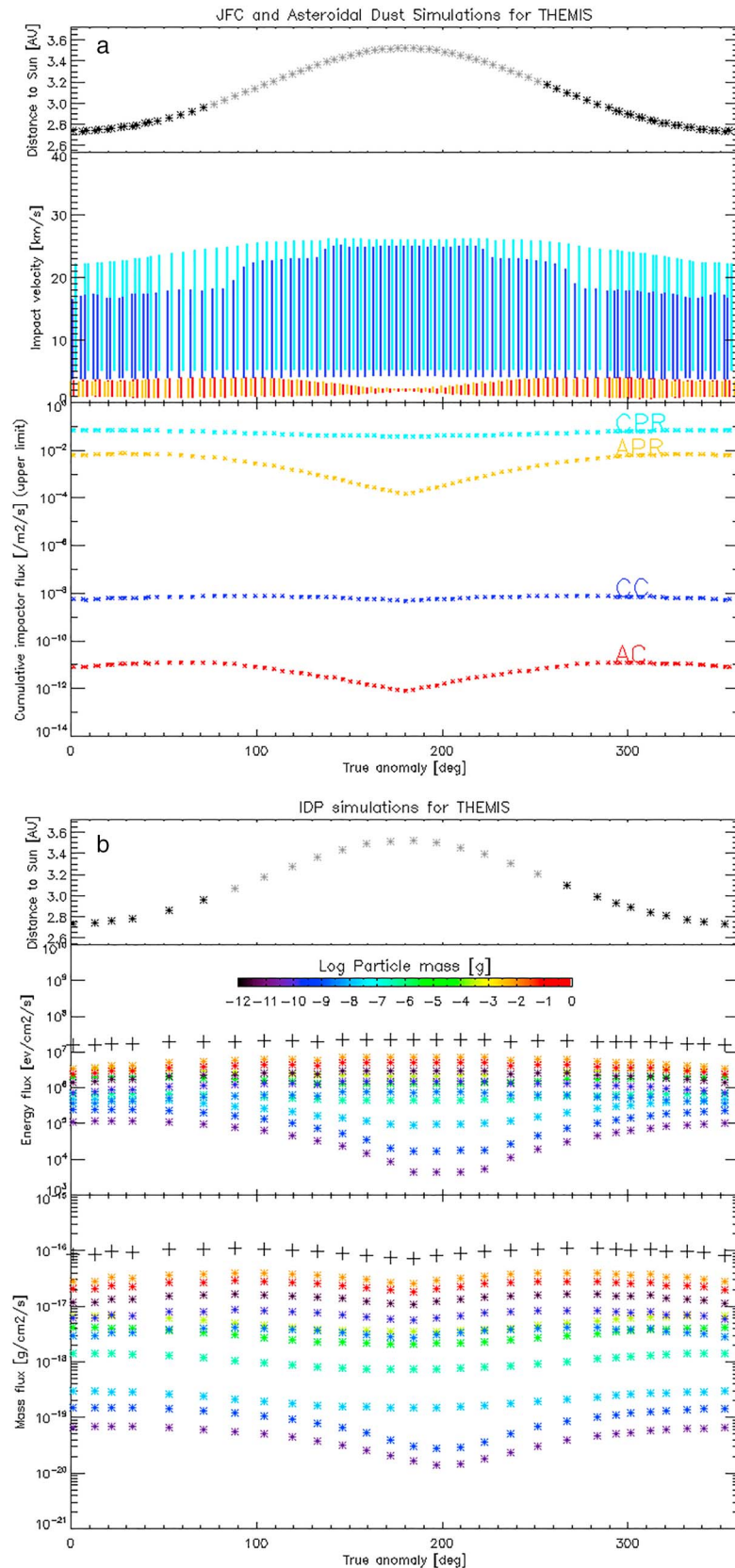


Figure A14. See Figure A1 caption.

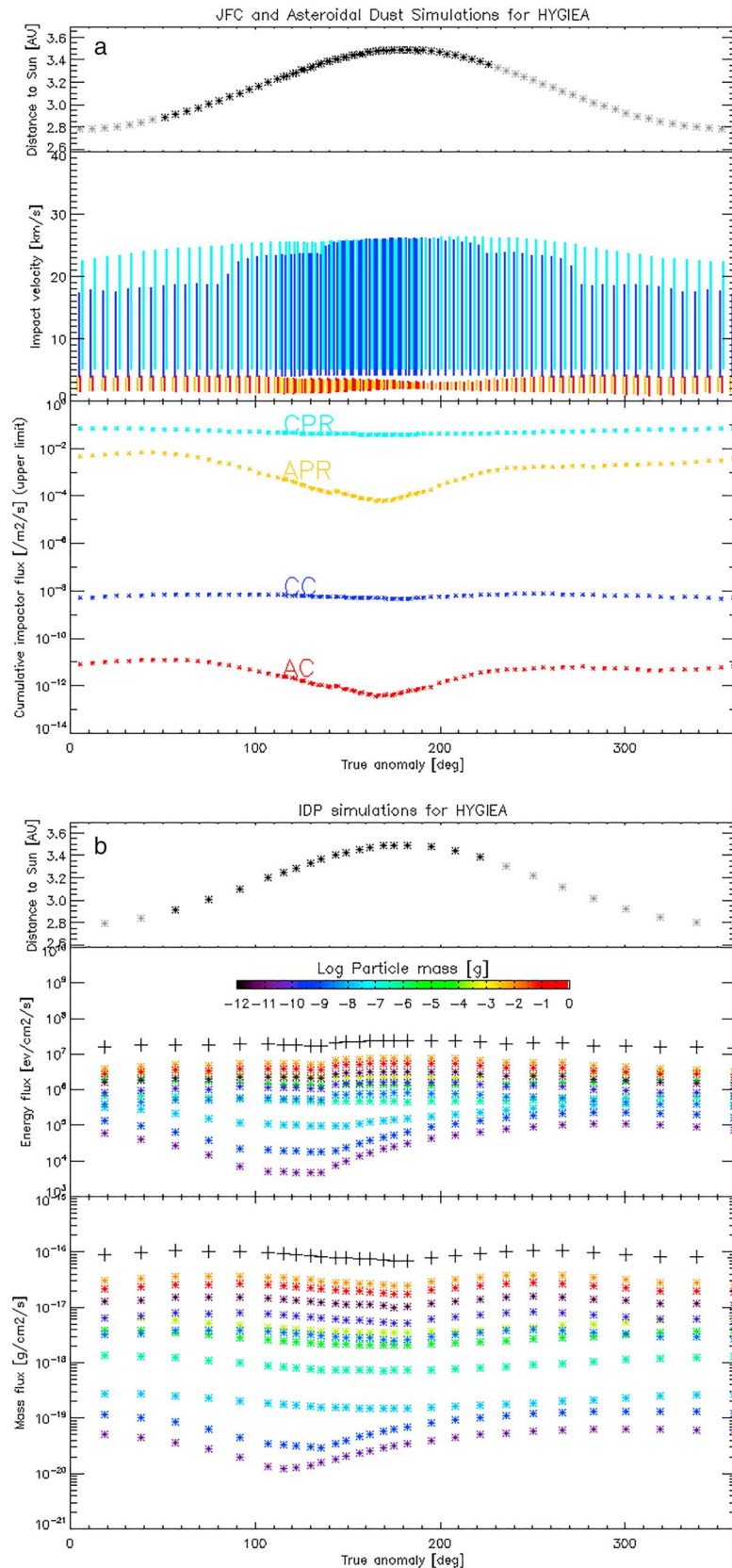


Figure A15. See Figure A1 caption.

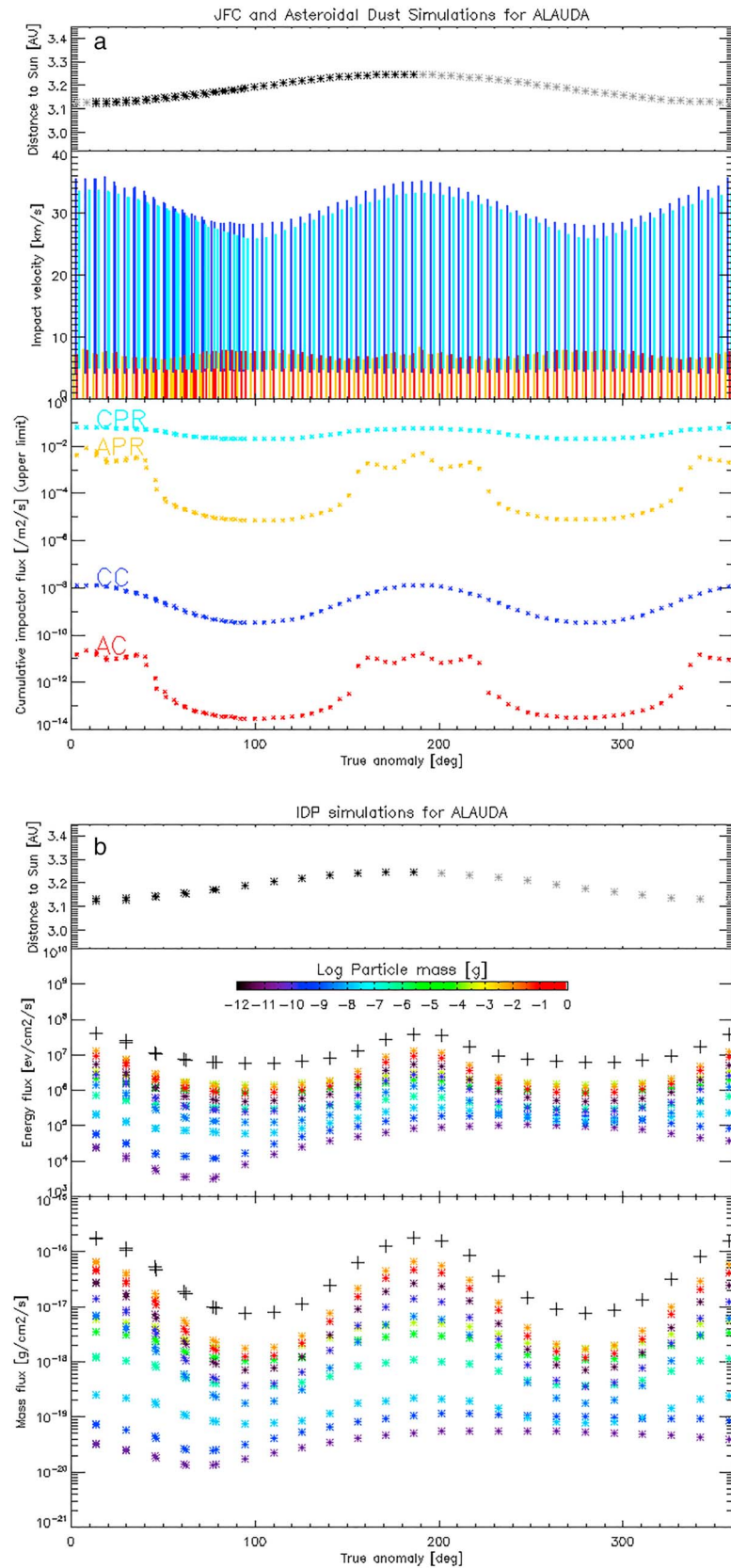


Figure A16. See Figure A1 caption.

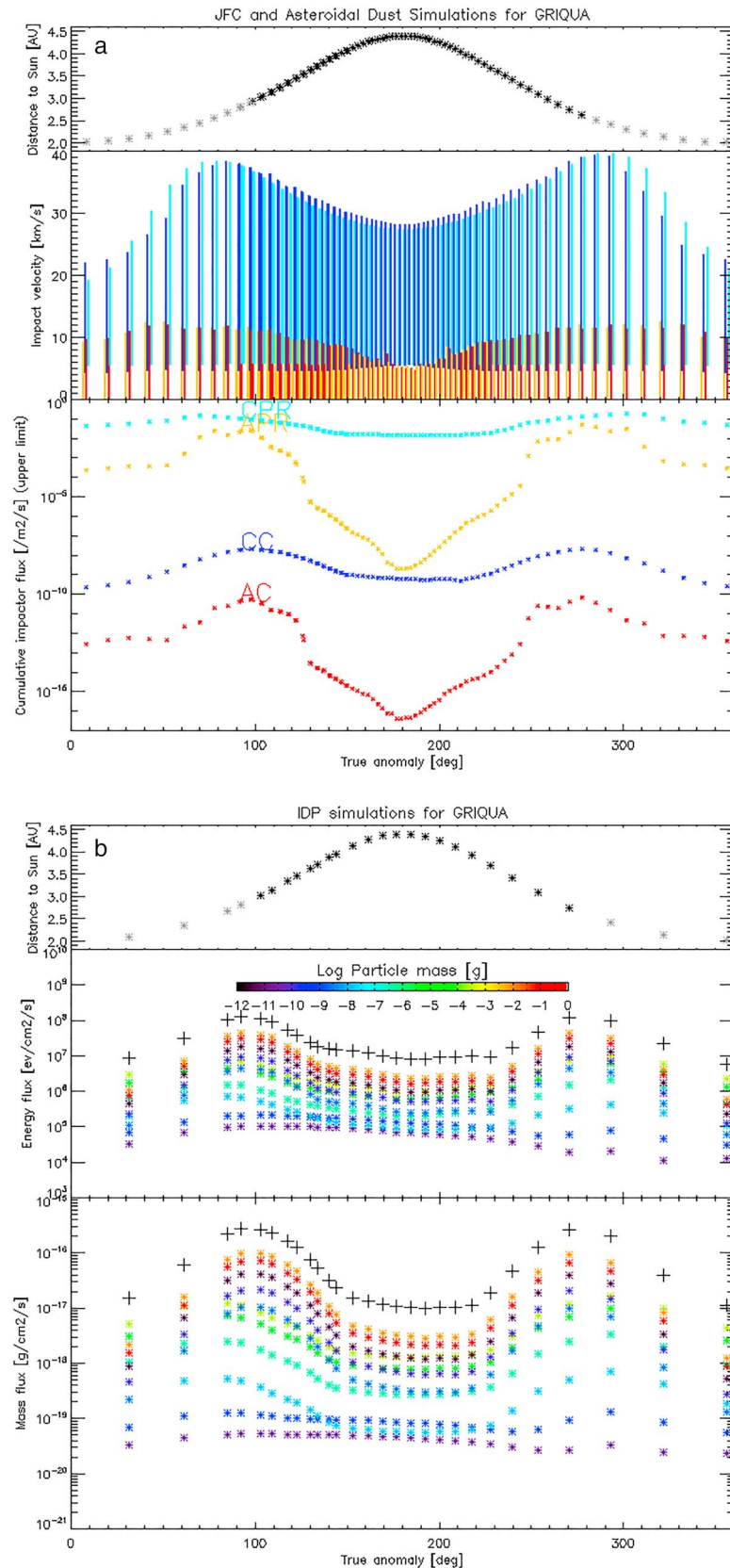


Figure A17. See Figure A1 caption.

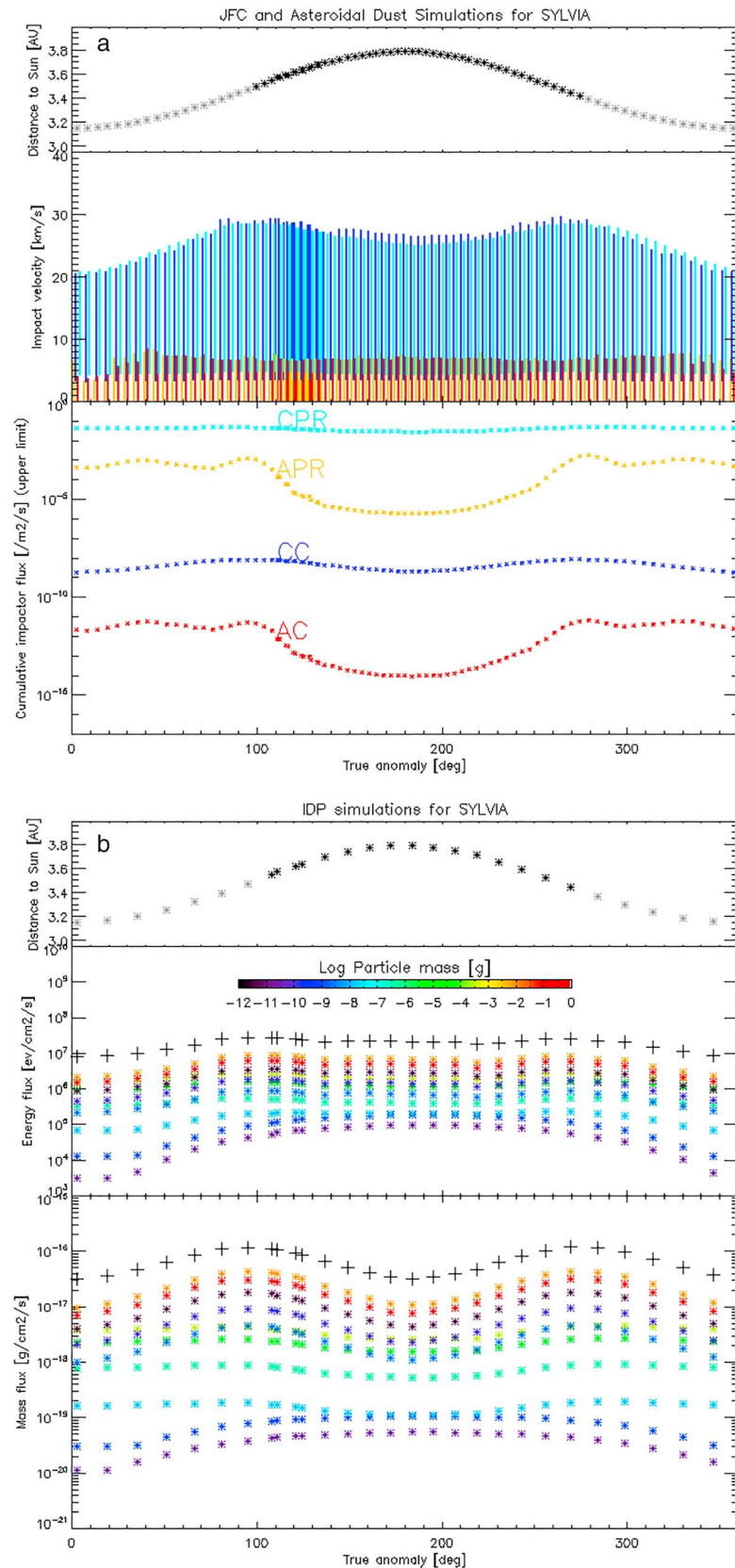


Figure A18. See Figure A1 caption.

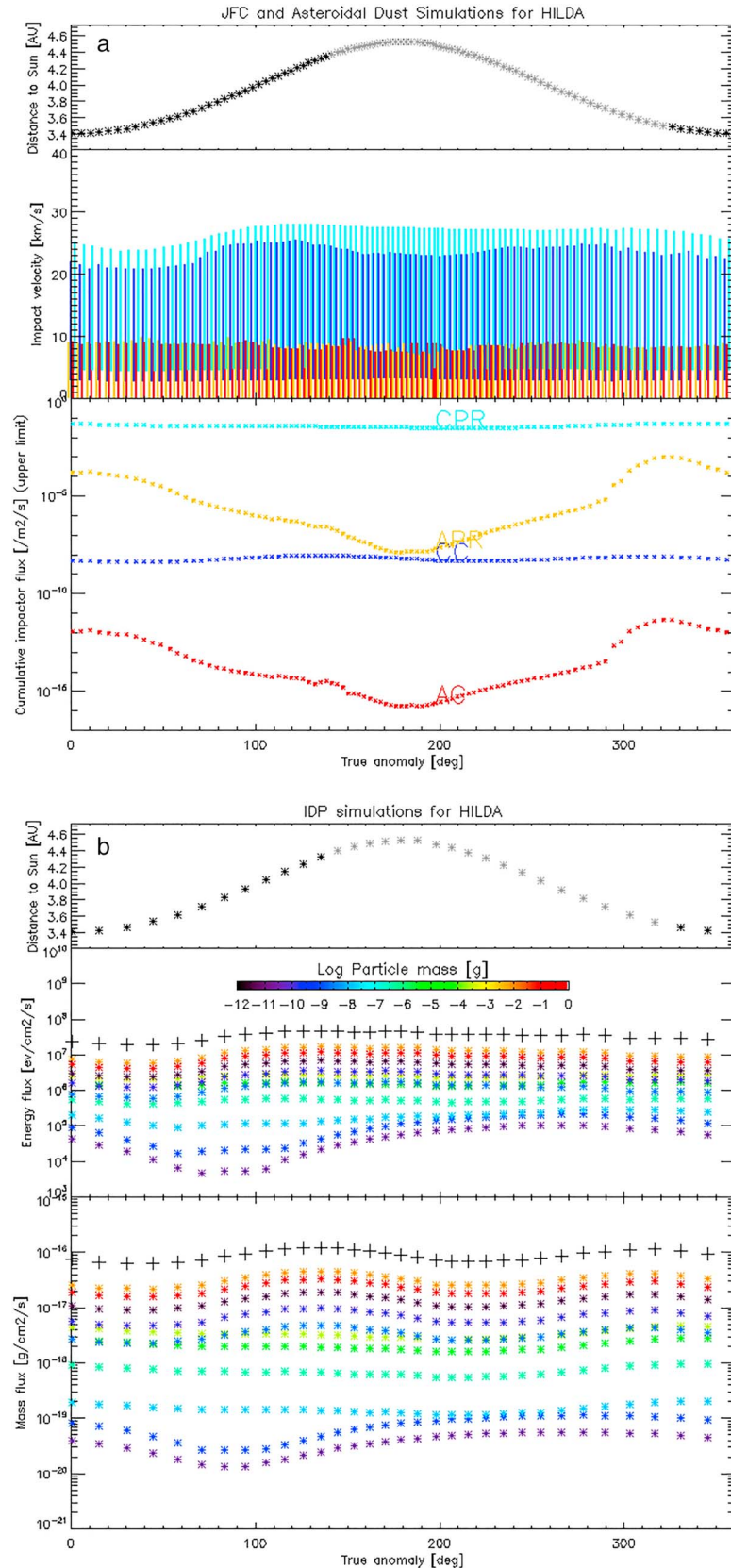


Figure A19. See Figure A1 caption.

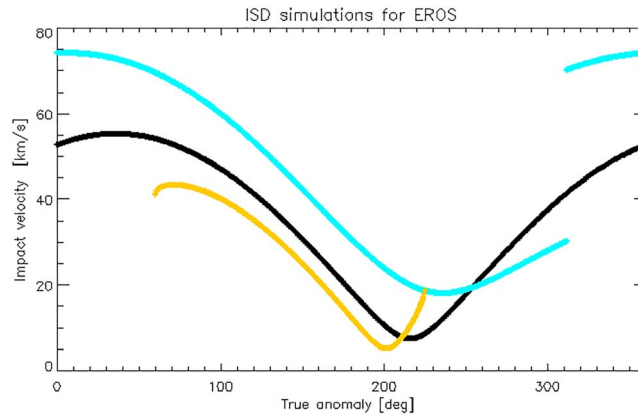


Figure A20. Impact velocity of interstellar dust (ISD) grains on the asteroid as function of the asteroid's position on its orbit, parameterized by the true anomaly. The different line colors correspond to different β values. Black stands for $\beta = 1$, blue for $\beta = 0.2$, and yellow for $\beta = 1.3$.

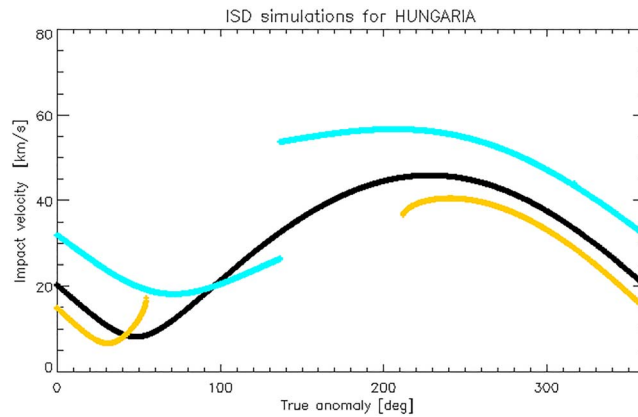


Figure A21. See Figure A20 caption.

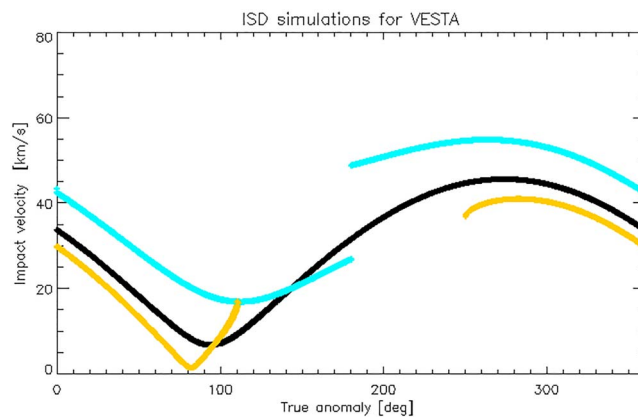


Figure A22. See Figure A20 caption.

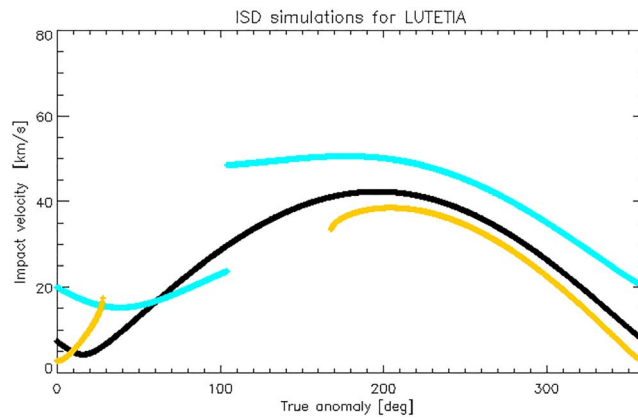


Figure A23. See Figure A20 caption.

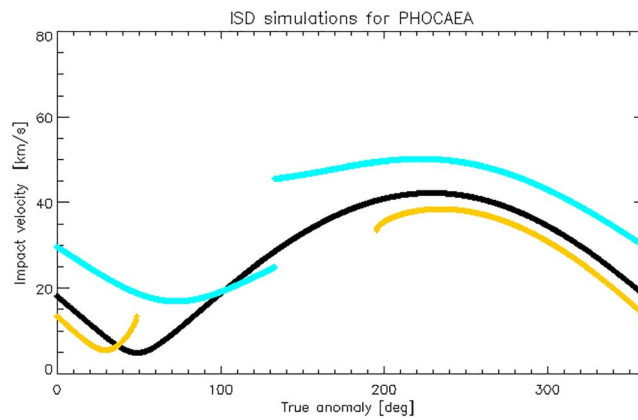


Figure A24. See Figure A20 caption.

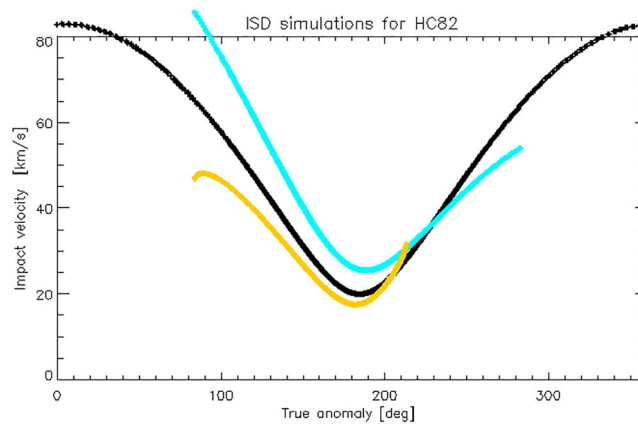


Figure A25. See Figure A20 caption.

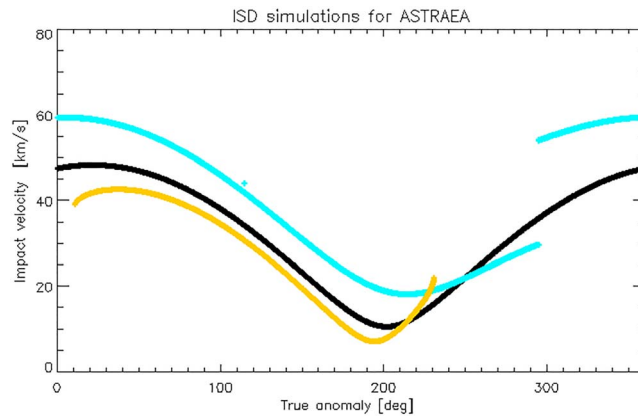


Figure A26. See Figure A20 caption.

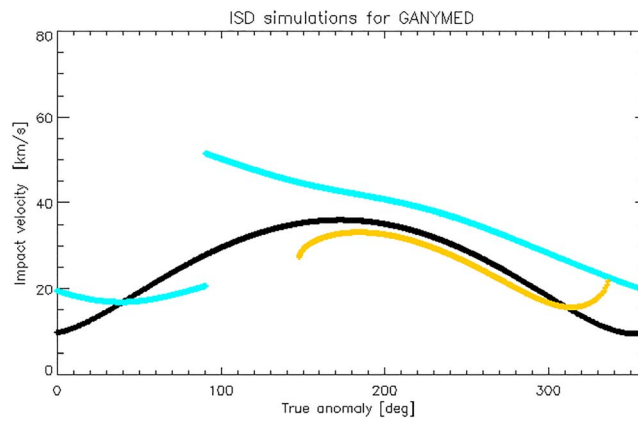


Figure A27. See Figure A20 caption.

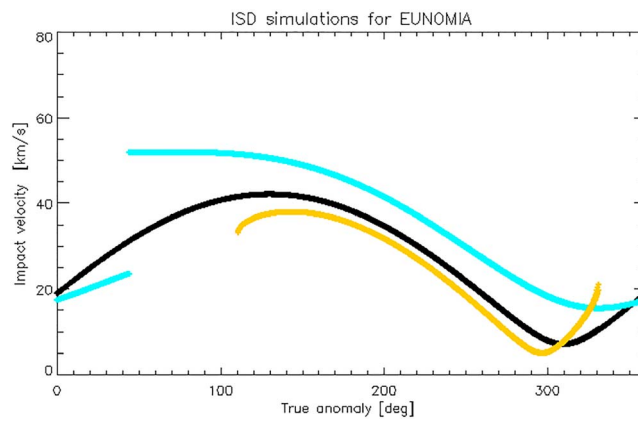


Figure A28. See Figure A20 caption.

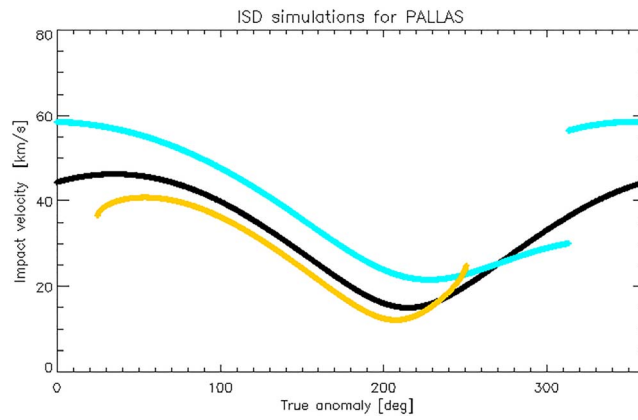


Figure A29. See Figure A20 caption.

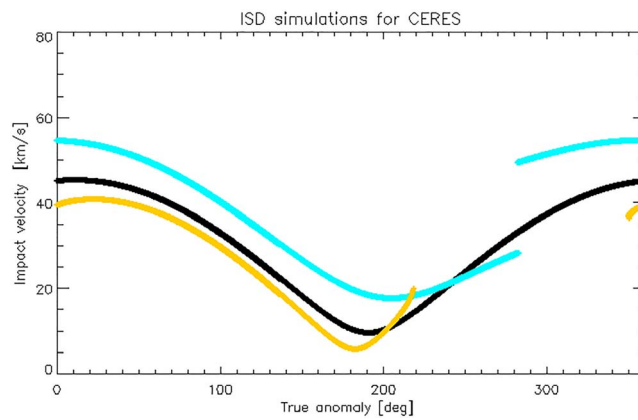


Figure A30. See Figure A20 caption.

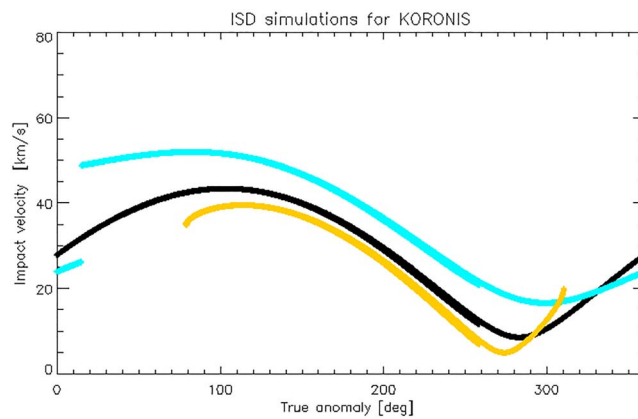


Figure A31. See Figure A20 caption.

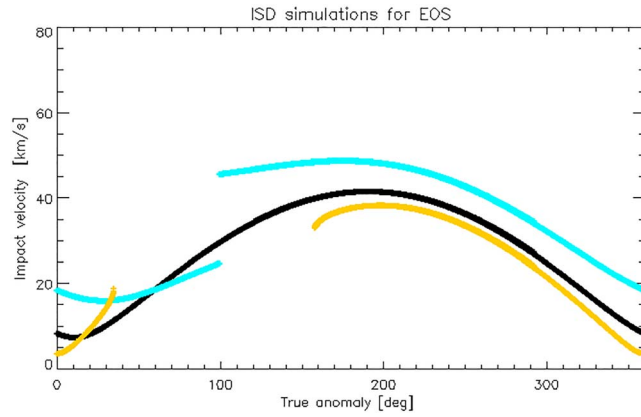


Figure A32. See Figure A20 caption.

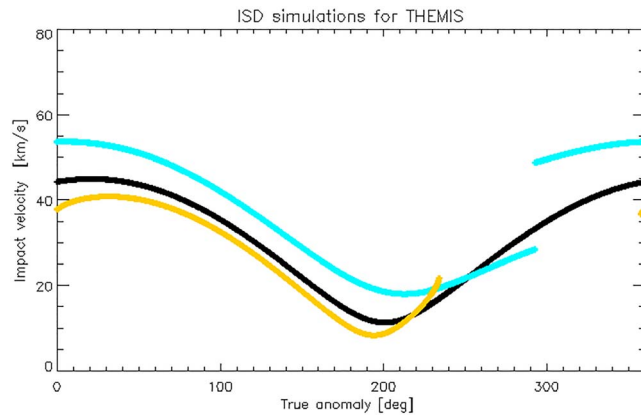


Figure A33. See Figure A20 caption.

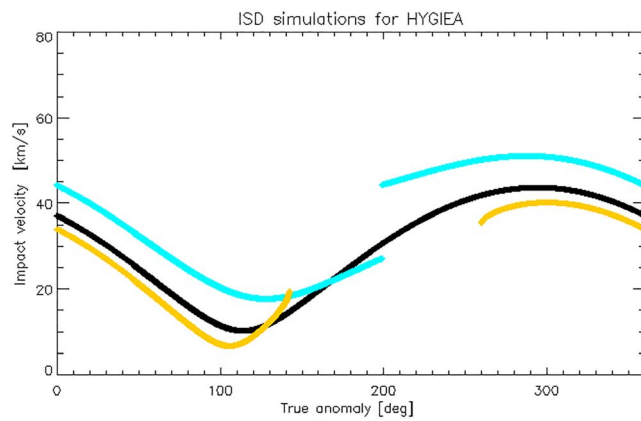


Figure A34. See Figure A20 caption.

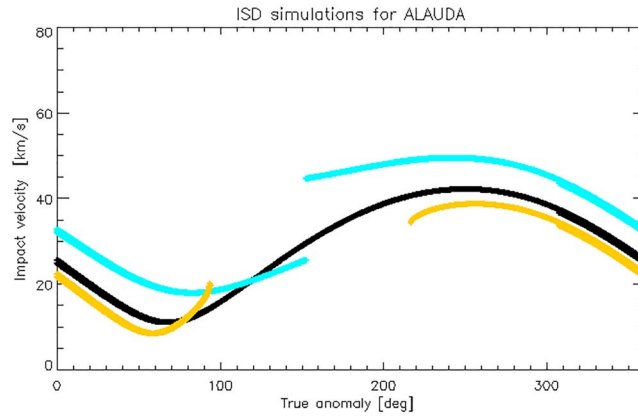


Figure A35. See Figure A20 caption.

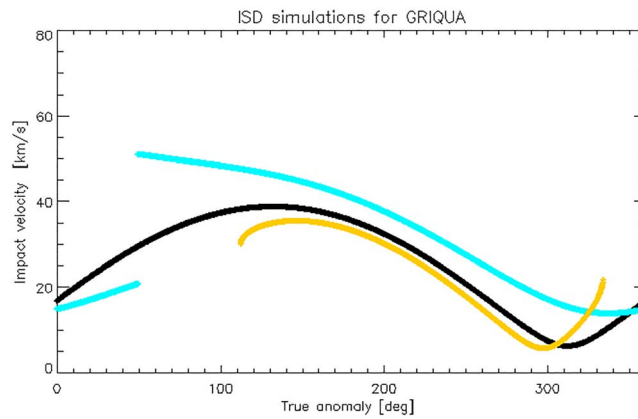


Figure A36. See Figure A20 caption.

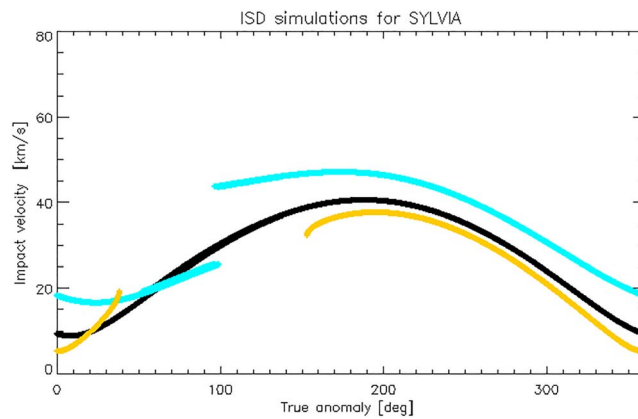


Figure A37. See Figure A20 caption.

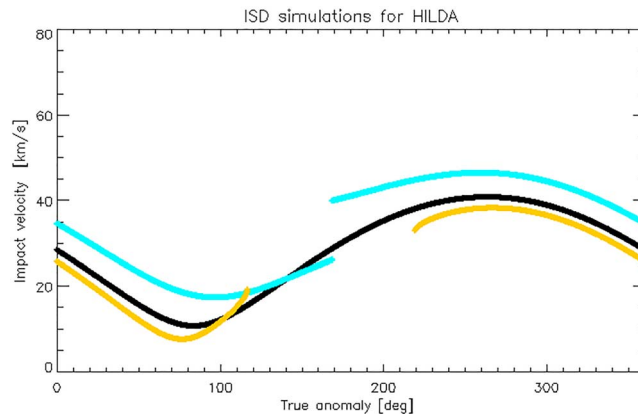


Figure A38. See Figure A20 caption.

Acknowledgments

N. Altobelli acknowledges support by the Science Faculty of the European Space Astronomy Center (ESAC). K. Fiege: This work was funded by Deutsche Forschungsgemeinschaft (DFG) under research Grant FI/2000. M. Trieloff acknowledges support by Klaus Tschira Stiftung gGmbH. The contribution from T. M. Orlando was carried out as part of REVEALS which was directly supported by the NASA Solar System Exploration Research Virtual Institute cooperative, agreement number NNA17BF68A. All ephemeris data used to generate the trajectories of the asteroids studied in this work can be found at the NASA Jet Propulsion Laboratory website (<https://ssd.jpl.nasa.gov/x/spk.html>). All model computations output can be found in the Figshare archive (<https://figshare.com/s/d675d8c44024e76626d6>).

References

- Ahrens, T. J., & O'Keefe, J. D. (1987). Impact on the Earth, ocean and atmosphere. *International Journal of Impact Engineering*, 5, 13–32.
- Altobelli, N., Dikarev, V., Kempf, S., Srama, R., Helfert, S., Moragas-Klostermeyer, G., et al. (2007). Cassini/Cosmic Dust Analyzer in situ dust measurements between Jupiter and Saturn. *Journal of Geophysical Research*, 112, A07105. <https://doi.org/10.1029/2006JA011978>
- Altobelli, N., Grün, E., & Landgraf, M. (2006). A new look into the Helios dust experiment data: Presence of interstellar dust inside the Earth's orbit. *Astronomy & Astrophysics*, 448, 243–252.
- Altobelli, N., Kempf, S., Krüger, H., Landgraf, M., Srama, R., & Grün, E. (2005). In situ monitoring of interstellar dust in the inner solar system. In C. C. Popescu & R. J. Tuffs (Eds.), *AIP Conf. Proc. 761: The Spectral Energy Distributions of Gas-Rich Galaxies: Confronting Models with Data* (pp. 149). College Park, MD
- Altobelli, N., Postberg, F., Fiege, K., Trieloff, M., Kimura, H., Sterken, V., et al. (2016). Flux and composition of interstellar dust at Saturn from Cassini's cosmic dust analyzer. *Science*, 352(6283), 312–318.
- Bennett, C. J., Pirim, C., & Orlando, T. M. (2013). Space-weathering of solar system bodies: A laboratory perspective. *Chemical Reviews*, 113, 9086–9150. <https://doi.org/10.1021/cr400153k>
- Berezhnoy, A. A., & Klumov, B. A. (2008). Impacts as sources of the exosphere on mercury. *Icarus*, 195, 511–522. <https://doi.org/10.1016/j.icarus.2008.01.005>
- Brunetto, R., Loeffler, M. J., Nesvorný, D., Sasaki, S., & Strazzulla, G. (2015). Asteroid surface alteration by space weathering processes. *Asteroids IV* (pp. 597–616). Tucson: University of Arizona Press. https://doi.org/10.2458/azu_uapress_9780816532131-ch031
- Colombo, G., Lautman, D. A., & Shapiro, I. I. (1966). The Earth's dust belt: Fact or fiction?, 2, Gravitational focusing and jacobi capture. *Journal of Geophysical Research*, 71, 5719.
- DeMeo, F. E., & Carry, B. (2013). The taxonomic distribution of asteroids from multi-filter all-sky photometric surveys. *Icarus*, 226, 723–741. <https://doi.org/10.1016/j.icarus.2013.06.027>
- DeMeo, F. E., & Carry, B. (2014). Solar system evolution from compositional mapping of the asteroid belt. *Nature*, 505, 629–634. <https://doi.org/10.1038/nature12908>
- Dikarev, V., Grün, E., Baggaley, J., Galligan, D., Landgraf, M., & Jehn, R. (2005). The new ESA meteoroid model. *Advances in Space Research*, 35, 1282–1289. <https://doi.org/10.1016/j.asr.2005.05.014>
- Divine, N. (1993). Five populations of interplanetary meteoroids. *Journal of Geophysical Research*, 17,029–17,048. <https://doi.org/10.1029/93JE01203>
- Fiege, K., Guglielmino, M., Altobelli, N., Trieloff, M., Srama, R., & Orlando, T. M. (2019). Space weathering induced via micro-particle impacts – Part 2: Dust impact simulation and meteorite target analysis. *Journal of Geophysical Research: Planets*, 124. <https://doi.org/10.1029/2018JE005564>
- Fulle, M., & Blum, J. (2017). Fractal dust constrains the collisional history of comets. *Monthly Notices of the Royal Astronomical Society*, 469, S39–S44. <https://doi.org/10.1093/mnras/stx971>
- Fulle, M., Corte, V. D., Rotundi, A., Weissman, P., Juhasz, A., Szego, K., et al. (2015). Density and charge of pristine fluffy particles from comet 67p/churyumov-gerasimenko. *The Astrophysical Journal Letters*, 802(1), L12.
- Grün, E., Staubach, P., Baguhl, M., Hamilton, D., Zook, H., Dermott, S., et al. (1997). South-north and radial traverses through the interplanetary dust cloud. *Icarus*, 129, 270–288.
- Grün, E., Zook, H., Baguhl, M., Balogh, A., Bame, S., Fechtig, H., et al. (1993). Discovery of Jovian dust streams and interstellar grains by the Ulysses spacecraft. *Nature*, 362, 428–430.
- Grün, E., Zook, H. A., Fechtig, H., & Giese, R. H. (1985). Collisional balance of the meteoritic complex. *Icarus*, 62, 244–272. [https://doi.org/10.1016/0019-1035\(85\)90121-6](https://doi.org/10.1016/0019-1035(85)90121-6)
- Grün, E., Zook, H., Fechtig, H., & Giese, R. (1985). Collisional balance of the meteoritic complex. *Icarus*, 62(May 1985), 244–272.
- Hilchenbach, M., Fischer, H., Langevin, Y., Merouane, S., Paquette, J., Rynö, J., et al. (2017). Mechanical and electrostatic experiments with dust particles collected in the inner coma of comet 67P by COSIMA onboard Rosetta. *Philosophical Transactions of the Royal Society of London Series A*, 375, 20160255. <https://doi.org/10.1098/rsta.2016.0255>
- Hornung, K., Merouane, S., Hilchenbach, M., Langevin, Y., Mellado, E. M., Della Corte, V., et al. Team, C O S I M A (2016). A first assessment of the strength of cometary particles collected in-situ by the COSIMA instrument onboard ROSETTA. *Planetary and Space Science*, 133, 63–75. <https://doi.org/10.1016/j.pss.2016.07.003>
- Juhász, A., & Horányi, M. (2013). Dynamics and distribution of nano-dust particles in the inner solar system. *Geophysical Research Letters*, 40, 2500–2504. <https://doi.org/10.1002/grl.50535>

- Kelsall, T., Weiland, J. L., Franz, B. A., Reach, W. T., Arendt, R. G., Dwek, E., et al. (1998). The COBE diffuse infrared background experiment search for the cosmic infrared background. II. Model of the interplanetary dust cloud. *Astrophysical Journal*, *508*, 44–73. <https://doi.org/10.1086/306380>
- Kimura, H., Mann, I., & Jessberger, E. K. (2003). Composition, structure, and size distribution of dust in the Local Interstellar Cloud. *The Astrophysical Journal*, *583*, 314–321. <https://doi.org/10.1086/345102>
- Koschny, D., & Grün, E. (2001). Impacts into ice-silicate mixtures: Crater morphologies, volumes, depth-to-diameter ratios, and yield. *Icarus*, *154*, 391–401. <https://doi.org/10.1006/icar.2001.6707>
- Krüger, H., Strub, P., Grün, E., & Sterken, V. J. (2015). Sixteen years of ulysses interstellar dust measurements in the solar system. I. Mass distribution and gas-to-dust mass ratio. *The Astrophysical Journal*, *139*. <https://doi.org/10.1088/0004-637X/812/2/139>
- Landgraf, M., Augustsson, K., Grün, E., & Gustafson, B. (1999). Deflection of the local interstellar dust flow by solar radiation pressure. *Science*, *286*(5448), 2319–2322.
- Landgraf, M., Krüger, H., Altobelli, N., & Grün, E. (2003). Penetration of the heliosphere by the interstellar dust stream during solar maximum. *Journal of Geophysical Research*, *108*(A10), 8030. <https://doi.org/10.1029/2003JA009872>
- Mann, I. (2010). Interstellar dust in the solar system. *Annual Review of Astronomy and Astrophysics*, *48*, 173–203. <https://doi.org/10.1146/annurev-astro-081309-130846>
- Nesvorný, D., Jenniskens, P., Levison, H. F., Bottke, W. F., Vokrouhlický, D., & Gounelle, M. (2010). Cometary origin of the zodiacal cloud and carbonaceous micrometeorites. Implications for hot debris disks. *The Astrophysical Journal*, *713*, 816–836. <https://doi.org/10.1088/0004-637X/713/2/816>
- Pokorný, P., Vokrouhlický, D., Nesvorný, D., Campbell-Brown, M., & Brown, P. (2014). Dynamical model for the toroidal sporadic meteors. *The Astrophysical Journal*, *789*, 25. <https://doi.org/10.1088/0004-637X/789/1/25>
- Poppe, A. R. (2016). An improved model for interplanetary dust fluxes in the outer Solar System. *Icarus*, *264*, 369–386. <https://doi.org/10.1016/j.icarus.2015.10.001>
- Staubach, P., Grün, E., & Jehn, R. (1997). The meteoroid environment near Earth. *Advances in Space Research*, *19*, 301–308. [https://doi.org/10.1016/S0273-1177\(97\)00017-3](https://doi.org/10.1016/S0273-1177(97)00017-3)
- Sterken, V. J., Altobelli, N., Kempf, S., Krüger, H., Srama, R., Strub, P., & Grün, E. (2013). The filtering of interstellar dust in the solar system. *Astronomy & Astrophysics*, *552*, A130. <https://doi.org/10.1051/0004-6361/201219609>
- Szalay, J. R., & Horányi, M. (2015). Annual variation and synodic modulation of the sporadic meteoroid flux to the Moon. *Geophysical Research Letters*, *42*, 10,580–10,584. <https://doi.org/10.1002/2015GL066908>
- Szalay, J. R., & Horányi, M. (2016). The impact ejecta environment of near earth asteroids. *Astrophysical Journal Letters*, *830*(L29). <https://doi.org/10.3847/2041-8205/830/2/L29>
- Tschauner, O., Sharp, T. G., & Stöffler, D. (2018). Introduction to the special issue of Meteoritics and Planetary Science on “Shock metamorphism and high pressure phases in meteorites and terrestrial impactites”. *Meteoritics and Planetary Science*, *53*, 3–4. <https://doi.org/10.1111/maps.13023>
- Vernazza, P., Binzel, R. P., Rossi, A., Fulchignoni, M., & Birlan, M. (2009). Solar wind as the origin of rapid reddening of asteroid surfaces. *Nature*, *458*, 993–995. <https://doi.org/10.1038/nature07956>